



Dr. F.M. Tesche  
Electromagnetics Consultant  
9308 Stratford Way  
Dallas, TX 75220 USA

Tel: (214) 956-9378  
Fax: (214) 956-9379  
E-Mail: [Tesche@ont.com](mailto:Tesche@ont.com)  
<http://www.tesche.com>

July 11, 1997

Dr Carl Baum  
Phillips Laboratory, PL/WSQW  
3550 Aberdeen Ave. SE  
Kirtland, AFB  
New Mexico 87117-5776

SSN 407

Subject: PxM Antenna Report #1

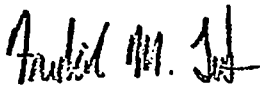
Dear Carl,

Enclosed please find a printable copy of a SSN note entitled *The PxM Antenna and Application to Radiated Field Testing of Electrical Systems, Part 1 - Theory and Numerical Simulations*. I have incorporated your comments into this revised report, and have reformatted it to be consistent with the SSN note requirements.

This is the first of a planned 2-part report, the second of which will be sent to you sometime in August. This particular report was partially funded by Armin Kaelin of the Swiss NEMP Laboratory, and it has been reviewed and approved for public release by the Swiss GRD.

Please note that I have left the note number blank. Either you can add the appropriate number to the title page, or once you assign a number, I will be happy to forward a new title page with the number included.

Sincerely,



Dr. Frederick M. Tesche  
EMC Consultant  
9308 Stratford Way  
Dallas, TX 75220

Sensor and Simulation Notes

Note 407

10 July, 1997

The PxM Antenna and Applications to  
Radiated Field Testing of Electrical Systems

Part-1 - Theory and Numerical Simulations

F.M. Tesche  
~~FE~~ Consultant  
Dallas, TX  
Tesche@ont.com

Abstract

*This report examines the EM fields produced by a pxm antenna, which consists of orthogonal electric and magnetic dipole elements operating together. At low frequencies, this antenna produces a radiation pattern having a maximum field in one direction and a wave impedance identical to that of a plane wave in free space. Moreover, the electromagnetic power density in the direction of the main lobe is real, indicating the absence of reactive power. Two different types of pxm antenna configurations are examined in this report, and a detailed numerical study of their radiating characteristics is presented.*

## Acknowledgment

This note arose from an interest in trying to understand and apply some early work by Dr. C. E. Baum in the use of low frequency radiators for the near-field illumination of electrical systems. Thanks are due to Dr. Baum for his many interesting ideas and discussions, to Dr. Torbjörn Karlsson of EMICON in Sweden for his interest in this work and for early attempts in p×m antenna measurements, and to Dr. Armin Kälin of the Swiss NEMP Laboratory for his support. This work was partially supported by the Swiss Defense Procurement Agency.

## Contents

1. Introduction	7
2. EM Fields Produced by Current and Charge Sources	8
2.1 Electric Dipole Fields	10
2.1.1 Far field approximations for the electric dipole	14
2.2 Magnetic Dipole Fields	14
2.2.1 Far field approximations for the magnetic dipole	16
2.3 The Ideal P×M Antenna	17
2.3.1 Far field approximations for the p×m source	23
3. The Combined Loop and Linear Element P×M Antenna	24
3.1 Antenna Geometry	24
3.2 Analysis of the Individual Antenna Components	25
3.3 Analysis of the Composite P×M Antenna	31
3.4 EM Fields Produced by the Wire-Loop Antenna	34
3.5 Effects of Impedance Loading	42
3.6 Radiation Efficiency	43
4. The Transmission Line P×M Antenna	44
4.1 Antenna Geometry	44
4.2 Analysis Methods	45
4.2.1 Transmission line model	45
4.2.2 Integral equation model	47
4.3 EM Fields from the Transmission Line Antenna	49
4.4 Radiation Efficiency	54
5. Conclusions	54
6. References	56

## Figures

- Figure 1. Geometry for calculating radiated E and H fields. (a) Coordinate system, (b) fields produced by a general current and charge distribution, (c) a low frequency approximation of the fields by elementary electric and magnetic dipoles. 9
- Figure 2. Examples of the dominant fields produced by a finite electric dipole (a) and a finite magnetic dipole (b). 10
- Figure 3. Plot of the spatial patterns of the total E-field from a point electric dipole at different normalized radial distances  $kr$ . 12
- Figure 4. Near field patterns for the  $E_\theta$ ,  $E_\phi$  and  $E_r$  components of the ideal  $p \times m$  antenna for various values of  $kr$ . 19
- Figure 5. Near field patterns for the  $H_\theta$ ,  $H_\phi$  and  $H_r$  components of the ideal  $p \times m$  antenna for various values of  $kr$ . 20
- Figure 6. Plot of the magnitude of the vertically polarized wave impedance as a function of  $kr$  along the  $x$ -axis. 21
- Figure 7. Three dimensional plot of the magnitude of the wave impedance  $Z_w^{(v)}$  for the vertically polarized E-field for the  $p \times m$  radiating element, shown as a function of the normalized radius,  $kr$ . (Note that only the front part of the impedance surface is illustrated.) 22
- Figure 8. The combined loop and linear element  $p \times m$  antenna. (a) The physical configuration of the antenna, (b) low frequency equivalent dipoles. 24
- Figure 9. Illustration of the charge separation for the calculation of  $p_z$  (part a), and the current flow for  $m_y$  (part b). 25
- Figure 10. Input admittance magnitude of the wire antenna with and without the parasitic loop antenna. 26
- Figure 11. Input admittance of the loop antenna with and without the parasitic wire antenna. 26
- Figure 12. Far field radiation patterns at different normalized frequencies,  $kh$ , for the isolated wire antenna of total length  $2h$ . 27
- Figure 13. Far field radiation patterns at different normalized frequencies,  $kh$ , for the wire antenna of total length  $2h$  with a parasitic loop. 28
- Figure 14. Far field radiation patterns at different normalized frequencies,  $kb$ , for the isolated loop antenna of radius  $b$ . 29
- Figure 15. Far field radiation patterns at different normalized frequencies,  $kb$ , for the loop antenna of radius  $b$  with a parasitic wire. 30

Figure 16. Plots of the ratio of the loop to wire voltage source strengths for the optimal p×m operation of the antenna, shown as a function of normalized frequency $kb$ .	32
Figure 17. The finite p×m antenna with voltage excitation on the linear antenna and current excitation on the loop.	33
Figure 18. Plots of the normalized ratio of the loop current source to the wire voltage source for optimal p×m operation of the antenna, shown as a function of normalized frequency $kb$ .	33
Figure 19. Far zone E-field radiation patterns at different normalized frequencies, $kb$ , for the wire-loop p×m antenna.	34
Figure 20. Plots of the $E_\theta$ , $E_\phi$ and $E_r$ near field components at various distances for a normalized frequency of $kb = 0.033\pi$ .	37
Figure 21. Plots of the $H_\theta$ , $H_\phi$ and $H_r$ near field components at various distances for a normalized frequency of $kb = 0.033\pi$ .	39
Figure 22. Plots of the wave impedance for the principal $E_\theta$ and $H_\phi$ fields for the loop, linear element and p×m antenna at normalized frequency $kb = 0.033\pi$ , as a function of position along the x-axis.	41
Figure 23. PxM radiating structure with sources with internal impedances $Z_{Wire}$ and $Z_{Loop}$ .	42
Figure 24. Plot of the ratio of loop to wire voltage for the p×m antenna for various loop source impedances.	42
Figure 25. Plot of the normalized frequency dependence of the normalized principal $E_\theta$ field from the loaded loop-wire p×m antenna at various distances along the x-axis.	43
Figure 26. Radiation efficiency of the loaded p×m antenna as a function of normalized frequency $kb$ .	44
Figure 27. Geometry of the transmission line p×m antenna.	45
Figure 28. Induced current, charge and dipole moments on the transmission line p×m antenna.	46
Figure 29. Computed input admittance magnitude of the transmission line p×m antenna using an integral equation analysis.	48
Figure 30. Far field radiation patterns for the transmission line p×m antenna as a function of normalized frequency, $kL$ .	50
Figure 31. Plots of the $E_\theta$ , $E_\phi$ and $E_r$ near field components at various distances $r$ for a normalized frequency $kL = 0.2\pi$ ( $f = 1$ MHz).	51
Figure 32. Plots of the $H_\theta$ , $H_\phi$ and $H_r$ near field components at various distances $r$ for a normalized frequency $kL = 0.2\pi$ ( $f = 1$ MHz).	52

- Figure 33. Plot of the wave impedance magnitude for the principal  $E_\theta$  and  $H_\phi$  components produced by the transmission line  $p \times m$  antenna along the  $x$ -axis, for different normalized frequencies  $kL$ . 53
- Figure 34. Plot of the normalized  $E_\theta$  field produced by the transmission line  $p \times m$  antenna at various radial distances along the  $x$ -axis, as a function of normalized frequency  $kL$ . 53
- Figure 35. Radiation efficiency of the transmission line  $p \times m$  antenna as a function of normalized frequency  $kL$ . 54

## 1. Introduction

Testing of electromagnetic (EM) responses in ground based facilities induced by the electromagnetic pulse (EMP) from a nuclear explosion, high-power microwave (HPM) weapons or natural threats, such as lightning, can often be done using a swept continuous wave (CW) EM field excitation [1]. This technique involves radiating an EM field at different frequencies and observing the induced internal responses in the facility, both in magnitude and phase.

While such testing is relatively straightforward at frequencies above about 30 MHz, there are difficulties in obtaining meaningful measurements at low frequencies. This is due to a number of reasons:

1. Antennas radiate poorly at low frequencies.
2. At low frequencies, the test object may be in the near field of the antenna. Moreover, the wave impedance of the excitation fields can be larger than the free space value of  $377 \Omega$  (for an electric dipole radiator), or it may be lower than this value (for a magnetic loop antenna).
3. It is difficult to produce a plane wave type field at low frequencies, not only due to the impedance fluctuations mentioned above, but also because other field components (i.e., cross polarized fields) may exist.

While these difficulties arise from fundamental constraints in the field radiation process, as described by Maxwell's equations, it is possible to improve on the simulation quality by considering a class of specially designed antennas. Known as the  $p \times m$  antenna, this type of radiator was proposed by Baum [2] for the purpose of improving the low frequency behavior of EMP simulators and other antennas.

The  $p \times m$  antenna is essentially a combination of an electric and magnetic dipole antenna which radiate fields having more desirable characteristics than would the single dipoles radiating alone. This concept has been studied theoretically by Yu [3] and has been applied to the design of radiating impulse-like antennas in [4, 5, and 6]. In addition, the  $p \times m$  theory has been applied to receiving antennas in the form of EM field sensors, as documented in [7 and 8].

The present report serves to review the basic theory behind this type of antenna, and to illustrate its radiation characteristics. In Section 2, the EM fields produced by a general distribution of electric charge and current are discussed, and then specialized to the case of simple electric and magnetic dipoles radiating in free space. Plots of the near and far fields from these idealized sources are presented to illustrate the spatial distribution of the EM fields away from the dipoles. Later, the  $p \times m$  combination of the electric and magnetic dipoles is investigated. The E- and H-fields produced by this

idealized point source combination are plotted for various observer distances, and the wave impedance for the primary field components is evaluated. In addition, expressions for the complex power in the EM field away from the sources are developed.

In Section 3, a physically realizable p×m antenna is analyzed using an integral equation solution. This antenna consists of a straight wire antenna coincident with a loop antenna, both of which are excited by independent voltage sources. The fields produced by these antennas are explored, and the proper ratio of antenna excitation voltages is determined to insure that the p×m radiation condition is met. Various E- and H-field patterns from this antenna are presented, and the primary field component wave impedance is plotted as a function of distance away from the antenna. These results may be compared with those of the idealized point p×m source to gain insight into the practical realization of this type of antenna.

Section 4 discussed the behavior of the traveling wave, or transmission line, antenna. This antenna is known as a Beverage antenna at higher frequencies, but at low frequencies, it acts as a p×m antenna, with the main radiation produced in the backward direction from the source, and with the correct free space wave impedance in the near zone. As in the case of the wire-loop antenna, the radiation efficiency of this antenna is very small, leading to possible difficulties in implementing this design in practical cases. Finally, Section 5 summarizes the important observations from this study and offers comments about the practical implementation of this antenna concept for EM test purposes.

## 2. EM Fields Produced by Current and Charge Sources

The evaluation of the EM fields produced by a set of time varying current and charge distributions  $\vec{J}(\vec{r})$  and  $\rho(\vec{r})$  shown in Figure 1 have been discussed in many different references [9-16]. Assuming a time harmonic variation of the form  $e^{j\omega t}$  (which is suppressed throughout this discussion), the E and H fields can be written as general integrals over the volumetric source distributions as

$$\vec{E}(\vec{r}) = \frac{-1}{\epsilon_0} \int_{\text{Vol}} \rho(\vec{r}') \frac{e^{-jkR}}{4\pi R} dv' - j\omega\mu_0 \int_{\text{Vol}} \vec{J}(\vec{r}') \frac{e^{-jkR}}{4\pi R} dv' \quad (1)$$

$$\vec{H}(\vec{r}) = \nabla \times \int_{\text{Vol}} \vec{J}(\vec{r}') \frac{e^{-jkR}}{4\pi R} dv', \quad (2)$$

where  $\vec{r}$  denotes the observer's location,  $\vec{r}'$  is the location of the current or charge source within the differential integration volume  $dv'$ , and  $R = |\vec{r} - \vec{r}'|$ . In these expressions,  $\omega$  is the radian frequency given by  $\omega = 2\pi f$ , the parameter  $k = \omega/c$  is the propagation constant in the space surrounding the sources,  $c = 3.0 \times 10^8$  m/s is the speed of light,  $\epsilon_0 = 8.85 \times 10^{-12}$  F/m is the free space permittivity, and  $\mu_0 = 4\pi \times 10^{-7}$  H/m is the permeability of free space.

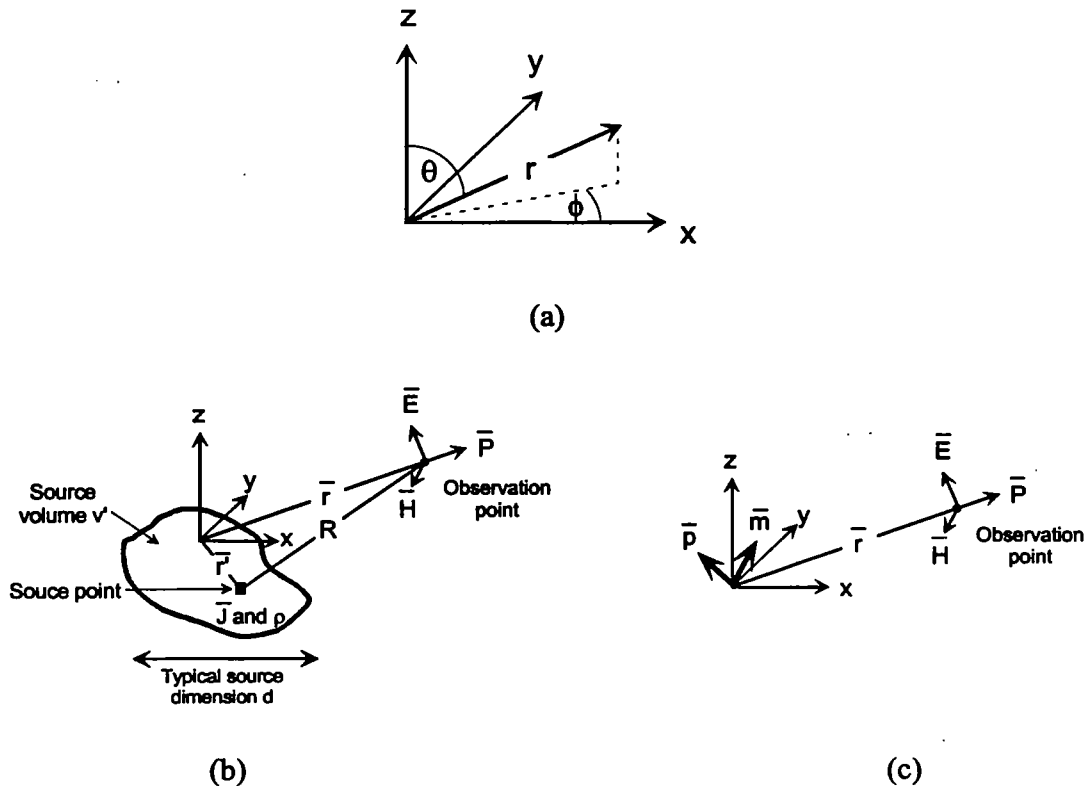


**Figure 1. Geometry for calculating radiated  $\mathbf{E}$  and  $\mathbf{H}$  fields. (a) Coordinate system, (b) fields produced by a general current and charge distribution, (c) a low frequency approximation of the fields by elementary electric and magnetic dipoles.**

Equations (1) and (2) are general in that they may be used for any frequency and for any distance of the observer, as long as the source current and charge distributions are known. It is possible, however, to simplify the task of determining the radiated fields in certain cases by considering expanding the current and charge into dipole and higher order multipoles. In this way the  $\mathbf{E}$  and  $\mathbf{H}$ -fields can be represented by an infinite sum of vector fields, each arising from the radiation of one of the multipoles [17].

This multipole representation for the fields is useful at “low” frequencies (when the typical dimension of the source region  $d$  in Figure 1b is much smaller than the wavelength, i.e.,  $kd = 2\pi d/\lambda \ll 1$ ), and for observation distances  $r \gg d$ . In this case, the radiated fields from the general source distribution can be approximated by the fields radiating from point electric and magnetic dipoles — the first terms in the general multipole expansion [3].

As discussed in [18], to be consistent with Maxwell’s equations, these dipole sources must produce both  $\mathbf{E}$  and  $\mathbf{H}$  fields. In the vicinity of the source, the  $\mathbf{E}$ -fields tend to be strongest for the electric dipole source, and conversely, the  $\mathbf{H}$ -fields are dominant for the magnetic dipole. Away from either dipole, the  $\mathbf{E}$  and  $\mathbf{H}$  fields approach the plane wave ratio of  $|\mathbf{E}|/|\mathbf{H}| = Z_0 \approx 377 \Omega$ , the impedance of free space.

As illustrated in Figure 2, the electric dipole can be thought of as arising from positive and negative charges  $q$ , separated by a distance  $2h$ . Similarly, the magnetic dipole can be considered as resulting from a current  $I$  flowing in a loop of radius  $b$ . As noted in the figure, as long as the observer is far from the sources (i.e., if  $r \gg 2h$  or  $r \gg b$ ), the shape of the lines of constant  $E$  and  $H$  are identical and appear to be produced by a single source located at the center of the distribution. Near to the sources, however, the details of the current or charge separations becomes important, and the field patterns are no longer the same. This illustrates the requirement that for a simple dipole representation of a current or charge distribution, it is important that the observation point be sufficiently far from the sources so that they appear as *point* sources.

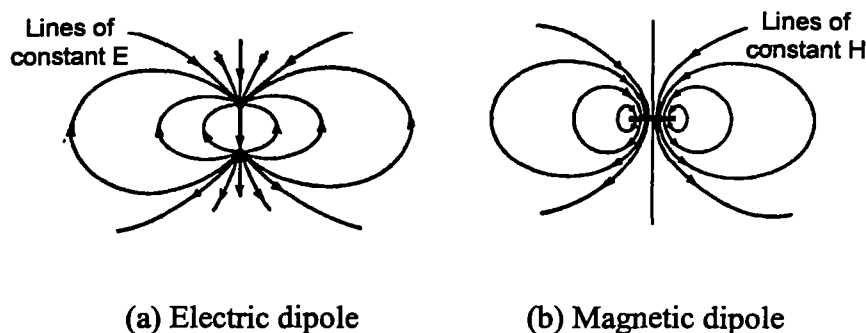


**Figure 2. Examples of the dominant fields produced by a finite electric dipole (a) and a finite magnetic dipole (b).**

The fields produced by these elementary dipole sources are important in describing the low frequency behavior of the  $p \times m$  antenna. Explicit expressions for both the  $E$  and  $H$  fields from these sources are reviewed in the following subsections.

### 2.1 Electric Dipole Fields

As discussed in [3] the electric dipole moment  $\vec{p}$  is defined in terms of a static moment of the electric charge density  $\rho$  as

$$\vec{p} = \int_{\text{sources}} \vec{r}' \rho(\vec{r}') dv' \quad (3)$$

For this dipole located at the origin of the coordinate system shown in Figure 1a, the vector  $E$  and  $H$  fields at an observation location  $\vec{r}$  are given by the expressions:

$$\vec{E}_e(\vec{r}) = -\frac{j\omega}{4\pi} Z_o \frac{e^{-jkr}}{r} \left[ \vec{p} G_2 - (\hat{r} \cdot \vec{p}) \hat{r} G_3 \right] \quad (4)$$

$$\vec{H}_e(\vec{r}) = -\frac{j\omega}{4\pi} \frac{e^{-jkr}}{r} \left[ (\hat{r} \times \vec{p}) G_1 \right] \quad (5)$$

where the following terms are used:

$$G_1 = \left( jk + \frac{1}{r} \right) \quad (6a)$$

$$G_2 = \left( jk + \frac{1}{r} + \frac{1}{jkr^2} \right) \quad (6b)$$

$$G_3 = \left( jk + \frac{3}{r} + \frac{3}{jkr^2} \right) \quad (6c)$$

$k = \omega/c$  and  $Z_0$  is the impedance of free space, given by  $Z_0 = \sqrt{\mu_0 / \epsilon_0} \approx 377 \Omega$ .

The fields produced by this source depend on both the spatial direction of the observer identified by the angles  $\theta$  and  $\phi$ , and on the distance  $r$  from the source. Consider as an example, a  $z$ -directed electric dipole moment  $p_z$ . In this case the E and H-fields are given by Eqs.(4) and (5) as

$$\vec{E}_e(\vec{r}) = -\frac{j\omega}{4\pi} Z_0 \frac{e^{-jkr}}{r} \left[ (G_2 - G_3) \cos\theta \hat{r} - G_2 \sin\theta \hat{\theta} \right] p_z \quad (7)$$

$$\vec{H}_e(\vec{r}) = \frac{j\omega}{4\pi} \frac{e^{-jkr}}{r} G_1 \sin\theta \hat{\phi} p_z. \quad (8)$$

To visualize the spatial distribution of the E-field from this source, consider the absolute value of the E-field  $E_{tot} = \sqrt{|E_x|^2 + |E_y|^2 + |E_z|^2}$ . Figure 3 presents the spatial distributions of  $E_{tot}$  for different values of the normalized distance from the source  $kr$ , ranging from  $kr = 0.1$  (i.e.,  $r \approx 0.63 \lambda$ ) to  $kr = 10,000$  ( $r \approx 63,000 \lambda$ ). Note that for very small  $kr$  the term  $(G_2 - G_3)$  dominates, and the E-field plot tends to resolve the two point sources that constitute the dipole, with the maximum value of E-field occurring along the  $z$ -axis. As the value of  $kr$  increases, the spatial pattern changes and slowly evolves into the toroidal radiation pattern that is commonly associated with the electric dipole. In the far zone for  $kr \gg 1$ , the pattern is seen to be very different from the near field because the term  $G_2$  is dominant. In this case, the radiation pattern has a null in the direction of the dipole, with a maximum of the field in the broadside direction.

For the  $z$ -directed electric dipole, the H-field behavior is much simpler than that of the E-field. From Eq.(8), it can be noted that the H-field has only a  $\phi$  component, and its spatial distribution remains constant as the observation distance  $kr$  is changed. Thus, the field pattern denoted as "far field" in Figure 3 also serves to describe the H-field pattern at any distance.

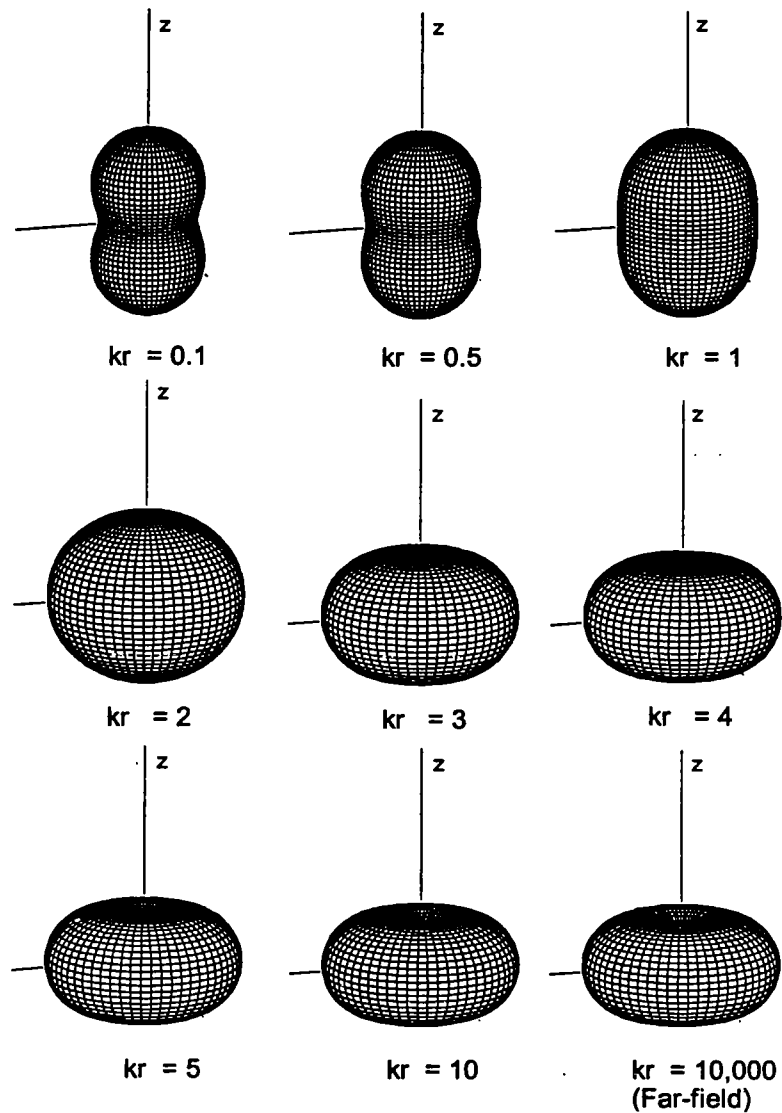


**Figure 3. Plot of the spatial patterns of the total E-field from a point electric dipole at different normalized radial distances  $kr$ .**

Away from the point electric dipole source,  $E_\theta$  and  $H_\phi$  are the principal components of the field. The ratio of these transverse fields can be thought of as defining a wave impedance  $Z_w$ , expressed as

$$Z_w = \frac{E_\theta}{H_\phi} = Z_o \frac{G_2}{G_1} = Z_o \left( 1 + \frac{1}{jkr(1 + jkr)} \right) \Omega. \quad (9)$$

Notice that this impedance is greater than the free space value of  $Z_o$ , signifying that the point electric dipole is a high impedance field source.

A useful quantity for describing the behavior of the EM fields surrounding the dipole source is the complex Poynting vector [19] defined as

$$\vec{P} = \vec{E} \times \vec{H}^* \quad (10)$$

This quantity can be used to calculate the total complex power  $\mathcal{W}$  passing through a closed surface surrounding the source. For a general field containing both  $\theta$  and  $\phi$  components of the E and H fields, this complex power is given by the integral of the radial component of  $\vec{P}$  as

$$\begin{aligned} \mathcal{W} &= \int_{\text{closed surface}} \vec{P} \cdot d\vec{s}' = \int_0^{2\pi} \int_0^\pi P_r r^2 \sin \theta d\theta d\phi \\ &= \int_0^{2\pi} \int_0^\pi (E_\theta H_\phi^* - E_\phi H_\theta^*) r^2 \sin \theta d\theta d\phi \end{aligned} \quad (11)$$

The real part of this complex power represents the time average power radiated away from the dipole:

$$\langle \mathcal{W}_{\text{real}} \rangle = \frac{1}{2} RE[\mathcal{W}] \quad (\text{Watts}), \quad (12)$$

while the imaginary part represents the reactive power in the near field:

$$\langle \mathcal{W}_{\text{img}} \rangle = \frac{1}{2} IM[\mathcal{W}] \quad (\text{Vars}). \quad (13)$$

This latter reactive power does no useful work, but represents a constraint on the radiating system in that its source must be able to support the current and the voltage levels needed for this reactive power, together with the real power.

From Eqs.(7) and (8), we see that the  $E_\phi$  and  $H_\theta$  field components are identically zero and the radial component of the Poynting vector is

$$\begin{aligned} P_r(\vec{r}) &= \left( \frac{\omega}{4\pi r} \right)^2 Z_o [G_2 G_1^*] |p_z|^2 \sin^2 \theta \\ &= \left( \frac{\omega}{4\pi r} \right)^2 Z_o |p_z|^2 \sin^2 \theta \left( k^2 + \frac{1}{jkr^3} \right) \end{aligned} \quad (14)$$

Notice that this expression contains both a real and imaginary part, indicating that the fields produced by the elementary electric dipole require the source to provide reactive and real power.

Integrating this quantity as indicated in Eq.(11) provides the total complex power in the field,

$$\mathcal{W} = \int_{\text{closed surface}} \bar{\mathbf{P}} \cdot d\mathbf{s}' = \frac{k^4 c^2 Z_o}{6\pi} p_z^2 \left( 1 - \frac{j}{(kr)^3} \right). \quad (15)$$

In this manner, the time averaged real power flowing away from the source is

$$\langle \mathcal{W}_{\text{real}} \rangle = \frac{k^4 c^2 Z_o}{12\pi} p_z^2 \quad (\text{Watts}) \quad (16)$$

and the reactive power contained in the fields at any distance  $r$  is

$$\langle \mathcal{W}_{\text{img}} \rangle = -\frac{k^4 c^2 Z_o}{12\pi (kr)^3} p_z^2 \quad (\text{Vars}). \quad (17)$$

This reactive power is a negative quantity, signifying that the source is essentially capacitive.

### 2.1.1 Far field approximations for the electric dipole

In the far field (or radiation zone) the terms  $G_i$  in the previous expressions can be simplified and the fields take on a simple form. Under the assumption that  $kr \gg 1$ , ( $G_2 - G_3$ )  $\rightarrow 0$  and  $G_1 \rightarrow G_2 \rightarrow jk$ . The radiated fields produced by the dipole source are

$$\bar{\mathbf{E}}_e(\bar{\mathbf{r}}) \approx -\frac{\mu_o}{4\pi} \omega^2 p_z \frac{e^{-jkr}}{r} \sin \theta \hat{\theta} \quad (18)$$

$$\bar{\mathbf{H}}_e(\bar{\mathbf{r}}) \approx -\frac{1}{4\pi c} \omega^2 p_z \frac{e^{-jkr}}{r} \sin \theta \hat{\phi}. \quad (19)$$

Note that the E and H fields are orthogonal and have a characteristic wave impedance of

$$Z_w = \frac{E_\theta}{H_\phi} = \frac{\mu_o}{c} = Z_o \approx 377 \, \Omega, \quad (20)$$

which is the plane wave impedance of free space. Moreover, in the far field, the power radiated by the field is given by Eq.(16), with no reactive component.

### 2.2 Magnetic Dipole Fields

The second basic elementary source of electromagnetic fields is the magnetic dipole. A magnetic dipole moment can be created simply by letting a quasistatic current  $I$  flow in a loop of radius  $b$ . In this case, the dipole moment is [18]

$$\bar{\mathbf{p}} = \pi b^2 I \hat{\mathbf{n}} = IA \hat{\mathbf{n}} \quad (21)$$

where  $\hat{n}$  is the unit normal to the surface of the loop and  $A$  is the loop area. For more complicated current distributions, ref.[3], defines the equivalent magnetic dipole moment by the integral

$$\vec{m} = \frac{1}{2} \int_{\text{sources}} \vec{r}' \times \vec{J}(\vec{r}') dv' . \quad (22)$$

In a manner similar to the electric dipole, the E and H-fields produced by this magnetic source can be expressed in terms as

$$\vec{E}_m(\vec{r}) = -\frac{j\omega}{4\pi} Z_c \frac{e^{-jkr}}{r} \left[ -\left( \hat{r} \times \frac{\vec{m}}{c} \right) G_1 \right] \quad (23)$$

$$\vec{H}_m = -\frac{j\omega}{4\pi} \frac{e^{-jkr}}{r} \left[ \frac{\vec{m}}{c} G_2 - \left( \hat{r} \cdot \frac{\vec{m}}{c} \right) \hat{r} G_3 \right], \quad (24)$$

where the terms  $G_i$  have been defined in Eqs.(6), and  $c$  is the speed of light  $c = 1/\sqrt{\mu_0 \epsilon_0}$ .

For the special case of a z-directed magnetic dipole,  $m_z$ , the fields in Eqs.(23) and (24) become

$$\vec{E}_m(\vec{r}) = -\frac{j\omega}{4\pi} Z_c \frac{e^{-jkr}}{r} \left[ G_1 \sin \theta \right] \hat{\phi} \frac{m_z}{c} \quad (25)$$

$$\vec{H}_m = -\frac{j\omega}{4\pi} \frac{e^{-jkr}}{r} \left[ (G_2 - G_3) \cos \theta \hat{r} - G_2 \sin \theta \hat{\theta} \right] \frac{m_z}{c} . \quad (26)$$

Note that the E-field in Eq.(25) is of the same form as the H-field for the electric dipole in Eq.(8), with the exception of a sign change and the free space impedance term,  $Z_0$ . Similarly, the H-field in Eq.(26) is of the same form as Eq.(7) for the E-field of the electric dipole. This is a consequence of electromagnetic reciprocity [9], and implies that the plots for the E-field in Figure 3 also describe the behavior of the H-field for the magnetic dipole source. Conversely, the plot of the E-field from this magnetic dipole will be the one labeled "far field" in Figure 3.

Away from this source, the  $E_\phi$  and  $H_\theta$  components dominate and the wave impedance  $Z_w$  becomes

$$Z_w = \frac{-E_\phi}{H_\theta} = Z_0 \frac{G_1}{G_2} = \frac{Z_0}{1 + \frac{1}{jkr(1+jkr)}}, \quad (27)$$

which has a value less than  $Z_0$ .

The radial component of the complex Poynting vector for this source is

$$\begin{aligned}
 P_r &= -E_\theta H_\theta^* = \left( \frac{\omega}{4\pi r} \right)^2 Z_o [G_1 G_2^*] \left| \frac{m_z}{c} \right|^2 \sin^2 \theta \\
 &= \left( \frac{\omega}{4\pi r} \right)^2 Z_o \left| \frac{m_z}{c} \right|^2 \sin^2 \theta \left( k^2 - \frac{1}{jkr^3} \right)
 \end{aligned} \tag{28}$$

which is seen to be the complex conjugate of  $P_r$  for the electric dipole moment in Eq.(14) with  $p_z$  replaced by  $m_z/c$ .

Integrating this quantity again as indicated in Eq.(11) provides the total complex power in the field,

$$\mathcal{W} = \int_{\text{closed surface}} \vec{P} \cdot d\vec{s} = \frac{k^4 Z_o}{6\pi} m_z^2 \left( 1 + \frac{j}{(kr)^3} \right). \tag{29}$$

In this manner, the time averaged real power flow is

$$\langle \mathcal{W}_{\text{real}} \rangle = \frac{k^4 Z_o}{12\pi} m_z^2 \text{ (Watts)} \tag{30}$$

and the reactive power at a distance  $r$  is

$$\langle \mathcal{W}_{\text{img}} \rangle = \frac{k^4 Z_o}{12\pi (kr)^3} m_z^2 \text{ (Vars)}. \tag{31}$$

This reactive power has a positive sign, which is typical of an inductive field arising from the low impedance current carrying loop.

### 2.2.1 Far field approximations for the magnetic dipole

Making the approximations that only the  $1/r$  terms in the field expressions contribute to the far fields, the radiation E and H components for the magnetic dipole become

$$\vec{E}_m(\vec{r}) \approx \frac{\mu_o}{4\pi} \omega^2 \frac{m_z}{c} \frac{e^{-jkr}}{r} \sin \theta \hat{\phi} \tag{32}$$

$$\vec{H}_m(\vec{r}) \approx -\frac{1}{4\pi c} \omega^2 \frac{m_z}{c} \frac{e^{-jkr}}{r} \sin \theta \hat{\theta}. \tag{33}$$

As in the electric dipole case, in the far zone the wave impedance for the magnetic dipole in Eq.(27) becomes equal to  $Z_o$  and the radiated power is given by Eq.(30).

### 2.3 The Ideal P×M Antenna

An interesting idea for combining electric and dipoles for an electrically small antenna has been proposed by Baum [2]. Consider the case illustrated in Figure 1b, in which a small electric dipole  $\vec{p}$  and a small magnetic dipole  $\vec{m}$  are used to approximate a more general distribution of current and charge. By superposition, the E and H-fields from these sources are given by

$$\vec{E}(\vec{r}) = \vec{E}_e(\vec{r}) + \vec{E}_m(\vec{r}) \quad (34)$$

$$\vec{H}(\vec{r}) = \vec{H}_e(\vec{r}) + \vec{H}_m(\vec{r}), \quad (35)$$

where the subscript  $e$  denotes the electric dipole component of the fields from the fields from Eqs.(4), (5), and  $m$  represents the fields from the magnetic source given by Eqs.(23) and (24).

Of special interest is when the  $\vec{p}$  and  $\vec{m}$  vectors are orthogonal — giving rise to the term “p×m”. Considering the special case of a z-directed  $\vec{p}$  and a y-directed  $\vec{m}$ , the total fields from this set of sources are expressed as

$$\vec{E}(\vec{r}) = -\frac{j\omega}{4\pi} Z_o \frac{e^{-jkr}}{r} \left[ (G_2 - G_3) p_z \cos \theta \hat{r} + \left( G_1 \frac{m_y}{c} \cos \phi - G_2 p_z \sin \theta \right) \hat{\theta} - G_1 \frac{m_y}{c} \cos \theta \sin \phi \hat{\phi} \right] \quad (36)$$

$$\vec{H}(\vec{r}) = -\frac{j\omega}{4\pi} \frac{e^{-jkr}}{r} \left[ (G_2 - G_3) \frac{m_y}{c} \sin \theta \sin \phi \hat{r} + G_2 \frac{m_y}{c} \cos \theta \sin \phi \hat{\theta} + \left( G_2 \frac{m_y}{c} \cos \phi - G_1 p_z \sin \theta \right) \hat{\phi} \right] \quad (37)$$

If we assume that the strengths of the  $\vec{p}$  and  $\vec{m}$  sources are related by

$$\frac{m_y}{c} = -p_z \quad (38)$$

the fields become

$$\vec{E}(\vec{r}) = -\frac{j\omega}{4\pi} Z_o \frac{e^{-jkr}}{r} \left[ (G_2 - G_3) \cos \theta \hat{r} - (G_1 \cos \phi + G_2 \sin \theta) \hat{\theta} + G_1 \cos \theta \sin \phi \hat{\phi} \right] p_z \quad (39)$$

$$\vec{H}(\vec{r}) = -\frac{j\omega}{4\pi} \frac{e^{-jkr}}{r} \left[ -(G_2 - G_3) \sin \theta \sin \phi \hat{r} - G_2 \cos \theta \sin \phi \hat{\theta} - (G_2 \cos \phi + G_1 \sin \theta) \hat{\phi} \right] p_z \quad (40)$$

These expressions contain all three vector components of E and H. However, in the far zone when  $kr \gg 1$ , the principal fields produced by this antenna are the  $E_\theta$  and  $H_\phi$  components. Moreover, in the far field the cross polarized  $E_\phi$  and  $H_\theta$  components may also exist. Additional details of the radiated fields from the pxm antenna are provided by Baum in [6], Eqs(6.3)-(6.5).

As an example of the fields produced by this p×m point source, Figure 4 plots the  $E_\theta$ ,  $E_\phi$  and  $E_r$  field components for  $kr = 0.1, 1, 10,$  and  $100,$  the latter which is denoted as the “far field” case. Figure 5 presents similar plots for the  $H_\theta$ ,  $H_\phi$  and  $H_r$  field components. In these plots, the relative sizes of the  $r$ ,  $\theta$  and  $\phi$  field components are consistent with each other for a particular value of the parameter  $kr$ . In this way, a relative comparison of the strengths of each field component can be made.

At observation locations close to the source (i.e., for small  $kr$ ), the largest fields are the radial components of  $E$  and  $H$ , with  $E$  being large along the  $z$  axis and  $H$  being large along the  $y$  axis. The principal tangential fields,  $E_\theta$  and  $H_\phi$ , occur along the  $x$ -axis and for small  $kr$ , these fields are large in both the  $+x$  and the  $-x$  directions. The cross polarized  $E_\phi$  and  $H_\theta$  fields, however, have a null in these directions, as do the radial  $E_r$  and  $H_r$  fields. This indicates that the fields along the  $x$ -axis are entirely transverse and appear to an observer like a local vertically polarized plane wave propagating away from the source.

As the observation point moves into the far field, the radial  $E$  and  $H$  components become vanishingly small and the fields become completely transverse with the primary components  $E_\theta$  and  $H_\phi$  having a large response in the  $+x$  direction and a null in the  $-x$  direction. Notice that the shape of the  $E_\phi$  component of the field does not change at all with the distance. That this observation is correct can be seen from the fact that the electric dipole produces no field component in this direction, and the only  $E$ -field component produced by the magnetic dipole has a distance independent pattern shape (see Eq.(25)). The same observation can be made regarding the  $H_\theta$  component. By taking the ratio of the two sets of transverse fields ( $E_\theta/H_\phi$ ) and ( $-E_\phi/H_\theta$ ), we can define two wave impedances

$$Z_w^{(v)} = \frac{E_\theta}{H_\phi} = Z_o \frac{G_1 \cos \phi + G_2 \sin \theta}{G_2 \cos \phi + G_1 \sin \theta} \quad (41a)$$

$$Z_w^{(h)} = \frac{-E_\phi}{H_\theta} = Z_o \frac{G_1}{G_2} \quad (41b)$$

where the superscript  $(v)$  has been used to denote the impedance for the vertically polarized field component (i.e., the field having an  $E_\theta$  component) and  $(h)$  denotes the horizontally polarized component (the field with  $E_\phi$ ). Notice that the impedance for horizontal polarization in Eq.(41b) is identical to that in Eq.(27) for the magnetic dipole source — a fact that is evident because this polarization results only from the magnetic dipole in the p×m combination. The impedance for the vertical portion of the field is different, however, because it arises from both the electric and magnetic terms of the source.

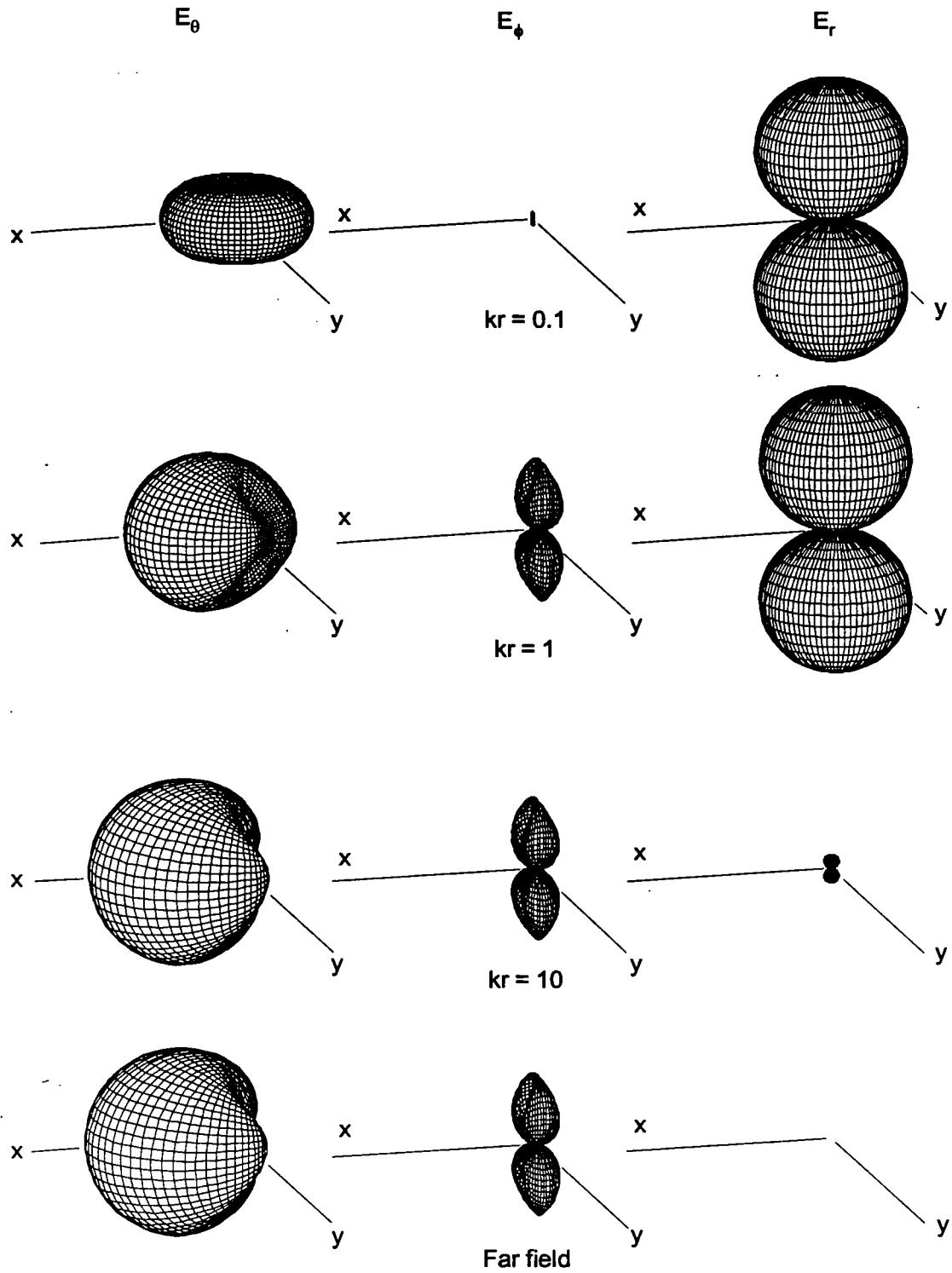
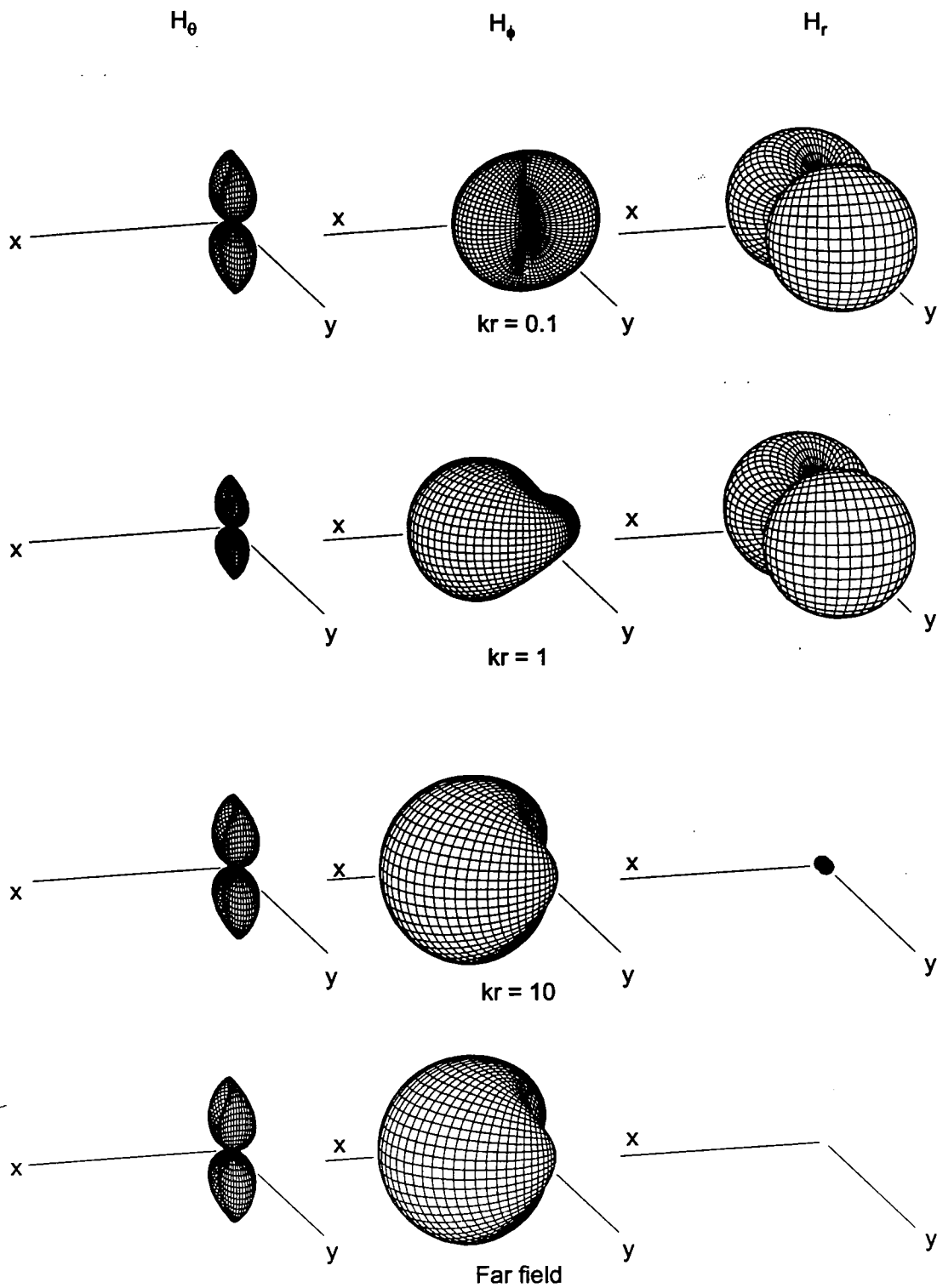


Figure 4. Near field patterns for the  $E_\theta$ ,  $E_\phi$  and  $E_r$  components of the ideal  $p \times m$  antenna for various values of  $kr$ .



**Figure 5. Near field patterns for the  $H_\theta$ ,  $H_\phi$  and  $H_r$  components of the ideal  $p \times m$  antenna for various values of  $kr$ .**

Along the  $x$ -axis,  $\sin\theta = 1$  and  $\cos\phi = 1$ , so that  $Z_w^{(v)} = Z_o$  for any observation location, *even in the near field*. Because  $(E_\phi$  and  $H_\theta)$  and  $(E_r$  and  $H_r)$  are zero on this axis, the fields appear like a transverse plane wave with the correct free space impedance near the sources. In the far field, note that both of the wave impedances are equal to  $Z_o$ , as required for a radiating antenna.

Figure 6 presents the magnitude of the wave impedance  $Z_w^{(v)}$  given in Eq.(9) for the electric dipole, in Eq.(27) for the magnetic dipole, and in Eq.(41a) for the primary fields from the p×m source, under the assumption that the observation location moves along the  $x$  axis. Note that near the source, the impedance changes dramatically for the electric or the magnetic dipole. For the point p×m source, however, this impedance is a constant 377  $\Omega$ .

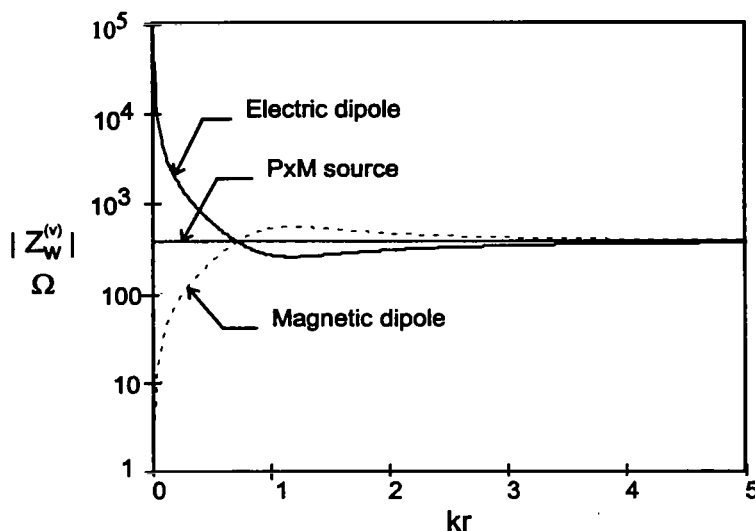


**Figure 6.** Plot of the magnitude of the vertically polarized wave impedance as a function of  $kr$  along the  $x$ -axis.

The wave impedance of the primary  $E_\theta$  and  $H_\phi$  fields varies with the observation angles  $\theta$  and  $\phi$  and with the distance from the source. Figure 7 illustrates spatial plots of the magnitude of  $Z_w^{(v)}$  for several different observation distances. In all cases, the impedance along the  $x$ -axis is 377  $\Omega$ . At low frequencies, this impedance is not isotropic, with a relatively large value occurring in the  $\phi = 90^\circ$  plane. As the frequency increases, however (or equivalently, as the distance  $r$  increases), the impedance becomes more isotropic, and in the far field, the impedance is a constant 377  $\Omega$  everywhere. The wave impedance of the cross polarized components is given by Eq.(41b) and is isotropic.

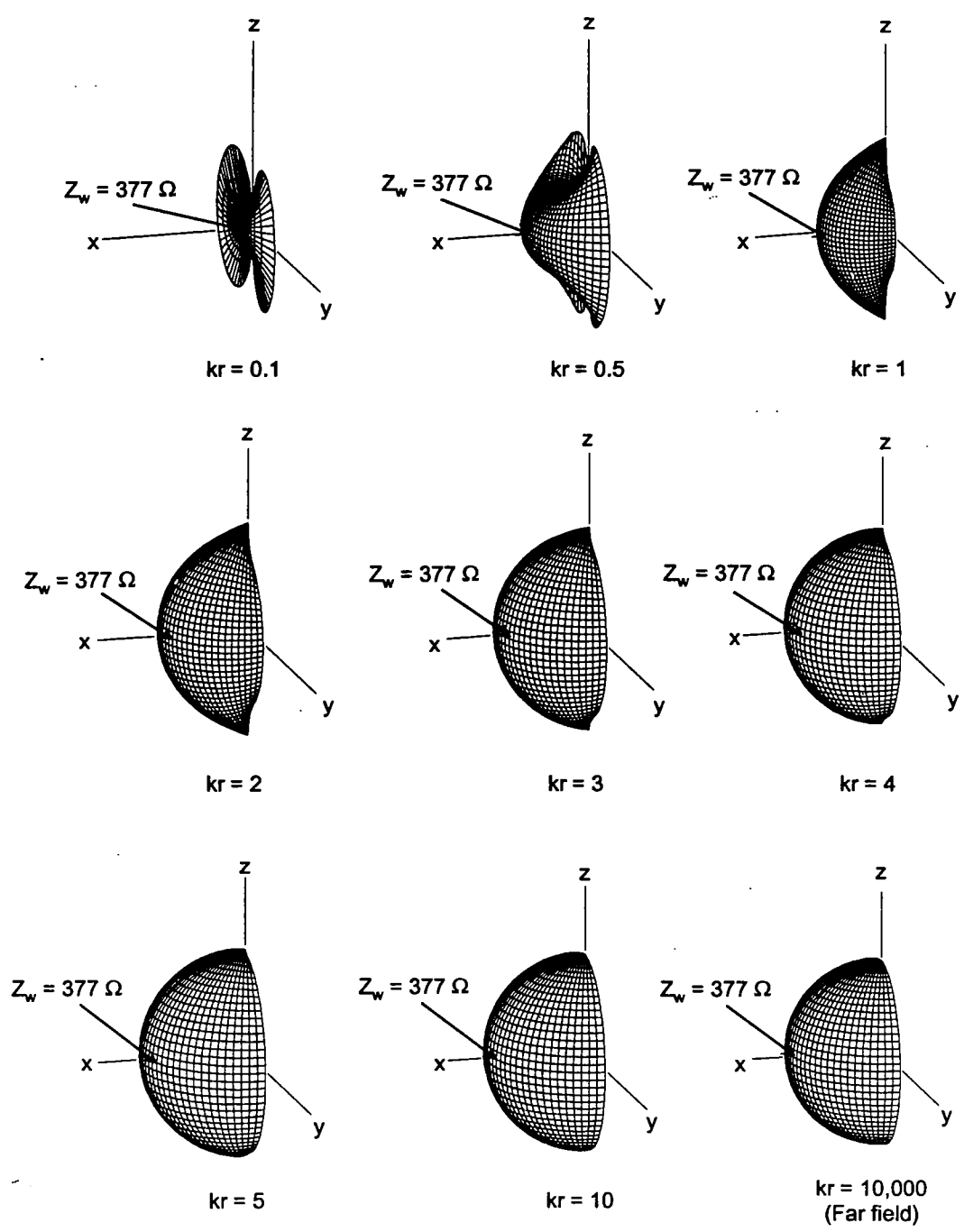


Figure 7. Three dimensional plot of the magnitude of the wave impedance  $Z_w^{(v)}$  for the vertically polarized E-field for the  $p \times m$  radiating element, shown as a function of the normalized radius,  $kr$ . (Note that only the front part of the impedance surface is illustrated.)

It is useful to compute the power of the EM field for this p×m source. The radial component of the Poynting vector is expressed as

$$P_r = \left( \frac{\omega}{4\pi r} \right)^2 Z_o \left[ (G_1 \cos \phi + G_2 \sin \theta)(G_2^* \cos \phi + G_1^* \sin \theta) + G_1 G_2^* \cos \theta \sin \phi \right], \quad (42)$$

and along the x axis, this becomes

$$\begin{aligned} P_r|_{x\text{-axis}} &= \left( \frac{\omega}{4\pi r} \right)^2 Z_o \left[ (G_1 + G_2)(G_2^* + G_1^*) \right] \\ &= \left( \frac{\omega}{4\pi r} \right)^2 Z_o |G_1 + G_2|^2 \end{aligned} \quad (43)$$

which is entirely real. There is no reactive power along this axis; however, in other radial directions from the source, a reactive power will exist. Integrating Eq.(42) over a sphere of radius  $r$  gives the expression for the total complex power

$$\mathcal{W} = \int_{\text{closed surface}} \bar{\mathbf{P}} \cdot d\mathbf{s}' = \frac{k^4 c^2 Z_o}{24\pi} p_z^2 \left( 7 - \frac{j}{(kr)^3} \right). \quad (44)$$

In this manner, the time averaged real power flow away from the source is

$$\langle \mathcal{W}_{\text{real}} \rangle = \frac{7k^4 c^2 Z_o}{48\pi} p_z^2 \quad (\text{Watts}) \quad (45)$$

which is 1.75 times the power radiated by the point electric dipole given in Eq.(16). The reactive power at a distance  $r$  is

$$\langle \mathcal{W}_{\text{img}} \rangle = -\frac{k^4 c^2 Z_o}{48\pi (kr)^3} p_z^2 \quad (\text{Vars}). \quad (46)$$

### 2.3.1 Far field approximations for the p×m source

In the far field simplifications to  $G_1$ ,  $G_2$  and  $G_3$  give rise to the following expressions for the fields

$$\vec{E}(\vec{r}) = \frac{-\omega^2}{4\pi c} Z_o \frac{e^{-jkr}}{r} \left[ (\cos \phi + \sin \theta) \hat{\theta} - \cos \theta \sin \phi \hat{\phi} \right] p_z \quad (47)$$

$$\vec{H}(\vec{r}) = \frac{-\omega^2}{4\pi c} \frac{e^{-jkr}}{r} \left[ \cos \theta \sin \phi \hat{\theta} + (\cos \phi + \sin \theta) \hat{\phi} \right] p_z, \quad (48)$$

from which it is immediately evident that  $Z_w^{(v)} = E_\theta/H_\phi = Z_o$  and  $Z_w^{(h)} = -E_\phi/H_\theta = Z_o$ .

### 3. The Combined Loop and Linear Element P×M Antenna

The radiation characteristics of the p×m dipoles discussed in the previous section are only idealizations of the low frequency behavior of an actual p×m antenna. Several different types of physical antenna configurations have been proposed by Baum [2], one of which is the combined loop and linear antenna. This antenna and its behavior are discussed in this section.

#### 3.1 Antenna Geometry

As shown in Figure 8a, this antenna consists of a thin wire of length  $2h$  and radius  $a$ , located along the  $z$  axis, together with a conducting loop located in the  $x$ - $z$  plane. The loop has a radius  $b$  and a wire radius  $a$ . The wire antenna is excited by a lumped voltage source  $V_{wire}$  at the midpoint of the wire, and the loop is excited by a similar voltage source of strength  $V_{Loop}$  at the  $x = b$  location on the loop. These sources act together to induce charge and current on the wires and these result in an electric and magnetic dipole moments  $p_z$  and  $m_y$ , as shown in Figure 8b.

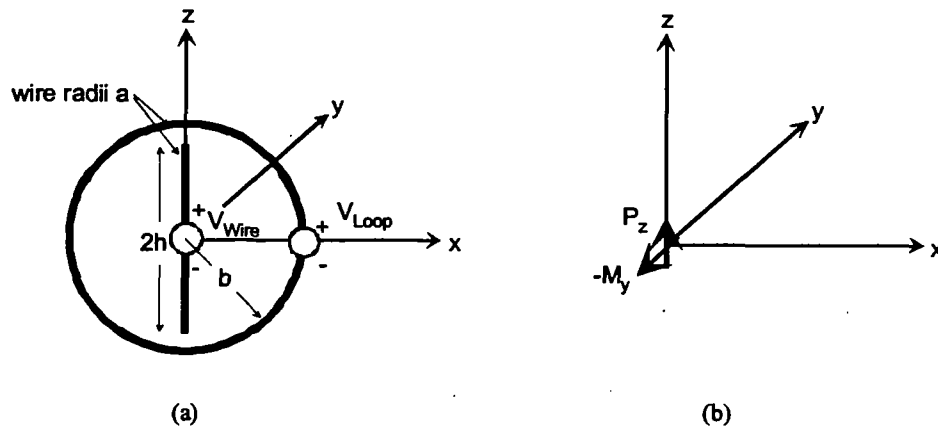
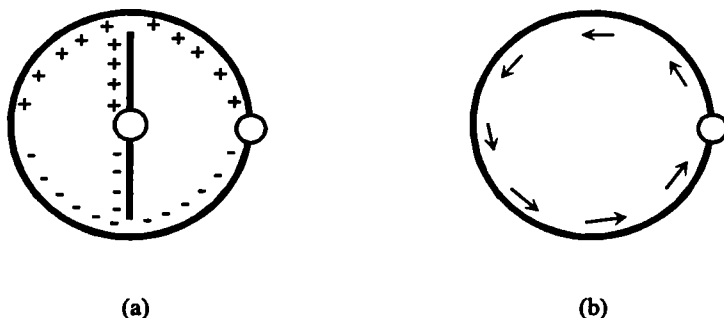


Figure 8. The combined loop and linear element p×m antenna. (a) The physical configuration of the antenna, (b) low frequency equivalent dipoles.

At low frequencies, the EM fields from this combined antenna can be computed from a knowledge of the electric and magnetic dipole moments given by Eqs.(3) and (22). As indicated in Figure 9a, the charge induced on the conductors appears on both the straight wire and on the loop, and as a result,  $p_z$  is a function of both of the source voltages,  $V_{Wire}$  and  $V_{Loop}$ . The magnetic dipole moment, however, depends only on the current flowing in the loop, as shown in Figure 9b, and as a result, it depends solely on the loop excitation voltage  $V_{Loop}$ . Although there is current induced in the straight wire, it is noted from Eq.(22) that the contribution from this current to the magnetic dipole moment is zero for a thin conductor, because the cross product is zero.



**Figure 9. Illustration of the charge separation for the calculation of  $p_z$  (part a), and the current flow for  $m_y$  (part b).**

### 3.2 Analysis of the Individual Antenna Components

The radiation from the antenna in Figure 8 has been discussed in [3]. In that analysis, however, the mutual coupling between the two antennas was neglected and a detailed examination of the fields produced by this antenna was not undertaken. Only the behavior of the various multipoles were presented. In the present study, we will continue the investigation of this p×m antenna and illustrate the behavior of the wave impedance and the field spatial patterns around the antenna. For this numerical study, a specific structure has been used:

- Loop radius  $b = 1$  m
- Wire length  $2h = 1.8$  m
- Conductor radii  $a = 0.2$  cm

Given a specification of the excitation voltages, it is possible to compute the induced current and charge on both conductors by an integral equation solution [9] which is subsequently solved numerically by the method of moments [20]. Several standard numerical codes are available for this purpose, one of which is the Numerical Electromagnetics Code (NEC) [21]. This code has been employed for the analysis described here.

An important aspect of this analysis is that the mutual coupling between the straight wire and loop antenna can be included. That such interaction is necessary can be noted in the plots in Figure 10, which illustrates the magnitude of the input admittance of the straight wire antenna, defined as  $Y_{in} = I_{Wire}/V_{Wire}$ , where  $I_{Wire}$  is the induced current at the input of the wire. This figure shows the admittance for the isolated straight wire (dotted line), together with the admittance of the wire and the unexcited loop antenna with its source terminals short circuited (solid line).

It is evident that the presence of the loop antenna has a marked effect on the input admittance, as well as on other near field quantities, such as the charge on the wires. In this plot, the peak of the response occurs at a normalized frequency of  $kh \approx \pi/2 = 1.57$ , or when the total length of the straight wire is about  $1/2$  wavelength long. With the loop

present, the input admittance is about a factor of 10 higher than for the isolated wire and there is a small bump in the response at  $kh \approx 1$  arising from a loop resonance occurring when the circumference equals a wavelength. We can conclude that it is important to consider mutual coupling effects in analyzing this antenna.

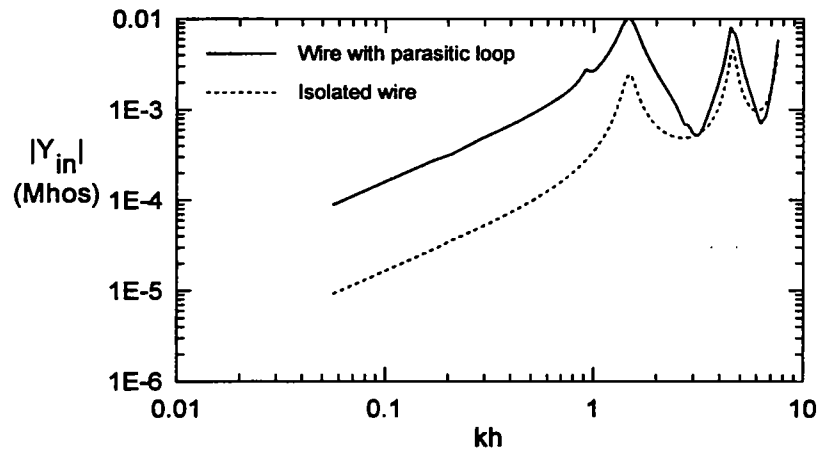


**Figure 10. Input admittance magnitude of the wire antenna with and without the parasitic loop antenna.**

The frequency behavior of the input admittance of the loop antenna with and without the unexcited parasitic wire antenna is illustrated in Figure 11. Here, we see that the loop has periodic resonances at frequencies where the circumference is an integral number of wavelengths. Because the total length of the loop is significantly longer than the wire antenna (6.28 m vs. 1.8 m) we note that the loop resonances occur at lower frequencies than for the wire antenna. In this plot, we see that the loop is not affected very much by the presence of the wire.

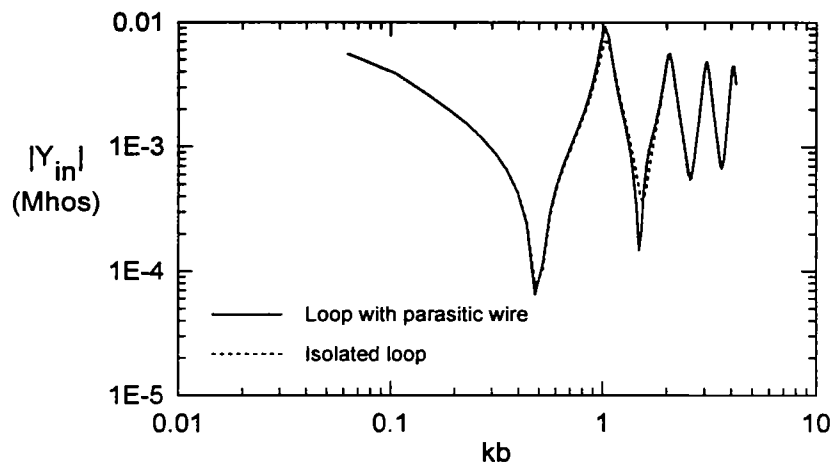


**Figure 11. Input admittance of the loop antenna with and without the parasitic wire antenna.**

It is instructive to show the far field radiation patterns for the various elements comprising the antenna, as well as for the complete antenna. As a first step, Figure 12 plots the spatial dependence of the radiation patterns for different values of normalized frequency  $kh$  for the isolated wire antenna. Because the antenna is located along the  $z$ -axis, symmetry requires no  $\phi$  variation of the fields. Moreover, only an  $E_\theta$  component of the E-field exists. Shown in this, and other plots of this type, are the *magnitudes* of the complex valued  $E_\theta$  and  $E_\phi$  field components, together with the total E-field,  $E_{tot}$ , defined as

$$E_{tot} = \sqrt{|E_\theta|^2 + |E_\phi|^2} \quad (49)$$

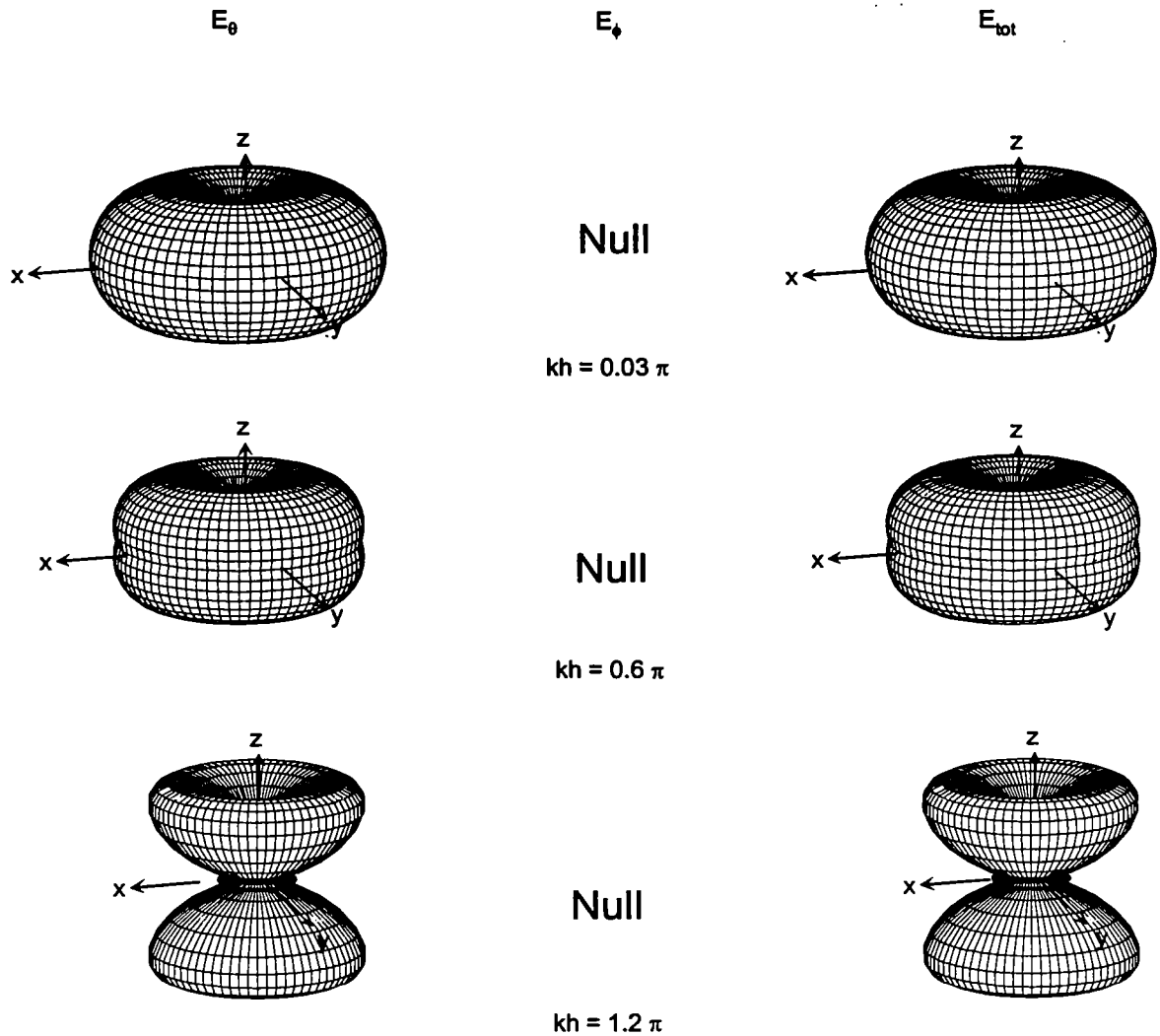


Figure 12. Far field radiation patterns at different normalized frequencies,  $kh$ , for the isolated wire antenna of total length  $2h$ .

At the relatively low frequency of  $kh = 0.03\pi$ , ( $f = 5$  MHz for the 1.8 m wire, which is well below the first resonance of the wire), the radiation pattern appears much like that in the far field for the ideal electric dipole shown in Figure 3. As the frequency increases, however, the radiation pattern begins to change and eventually “side lobes” begin to appear. At a normalized frequency of  $kh = 1.2\pi$ , well above the first antenna resonance, it is clear that this antenna structure is not behaving like a simple electric dipole; higher order multipoles have been excited and are needed to adequately represent the fields.

The effects of adding the unexcited parasitic loop antenna to the linear antenna are illustrated in Figure 13 for the same set of normalized frequencies used in Figure 12. Notice that in this case, there is a small  $E_\phi$  component to the field, in addition to the  $E_\theta$  field. At low frequencies, the shape of the principal E-field component  $E_\theta$  is still like that of the isolated wire. However, as the frequency increases, it is evident that the parasitic loading of the loop antenna has significantly altered the shape of the radiated field.

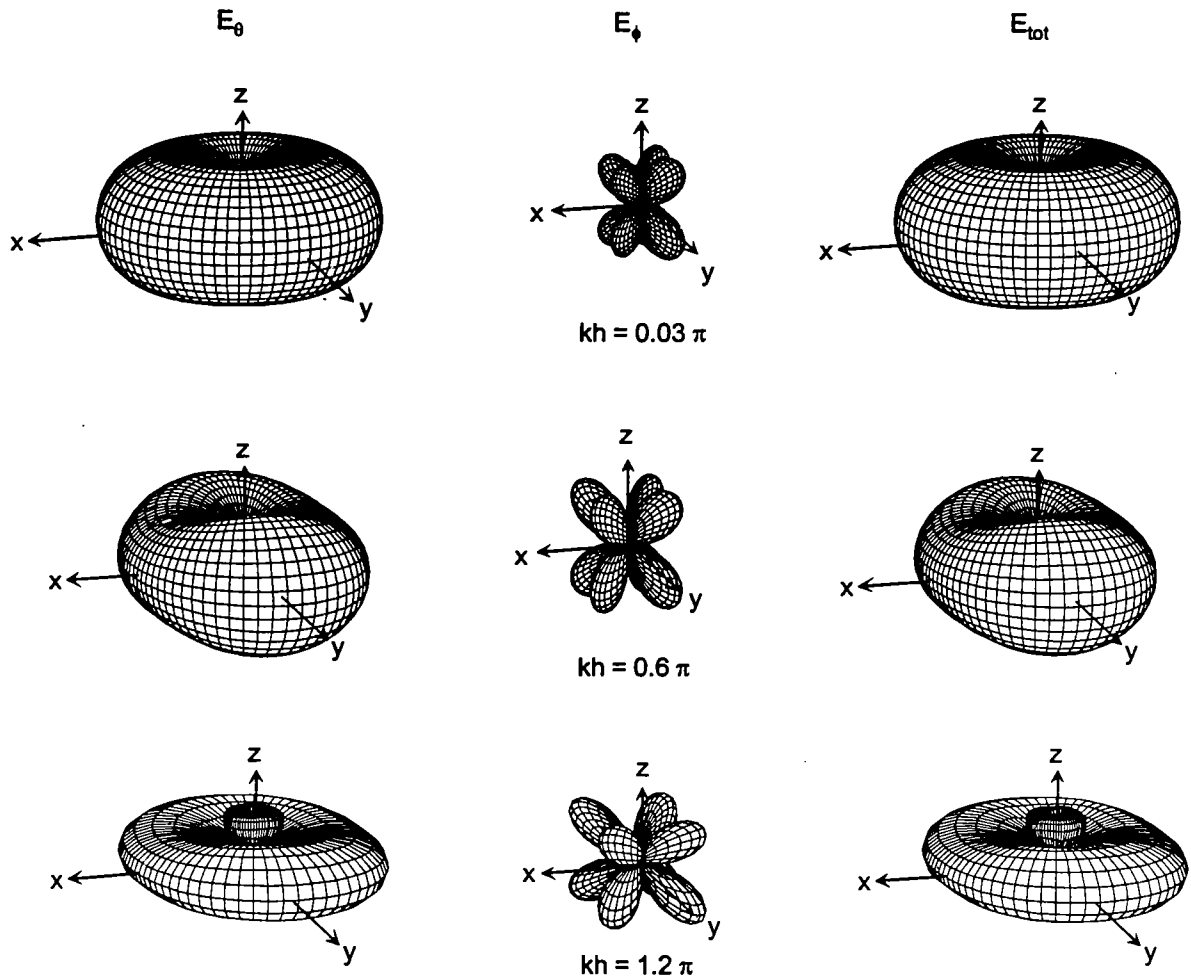


Figure 13. Far field radiation patterns at different normalized frequencies,  $kh$ , for the wire antenna of total length  $2h$  with a parasitic loop.

Similar plots for the excited loop antenna, without and with the unexcited parasitic wire antenna, are shown in Figure 14 and Figure 15, respectively. In this case, the normalized frequency is  $kb$ , which is related to the characteristic size of the loop. In these plots, it is evident that the mutual coupling between the loop and the wire is not very important and that the field patterns for the two cases are virtually identical. As in the case of the wire antenna, at low frequencies, the fields appear like that of the magnetic dipole. However, as the frequency increases, the higher order multipoles become important and the field shape changes.

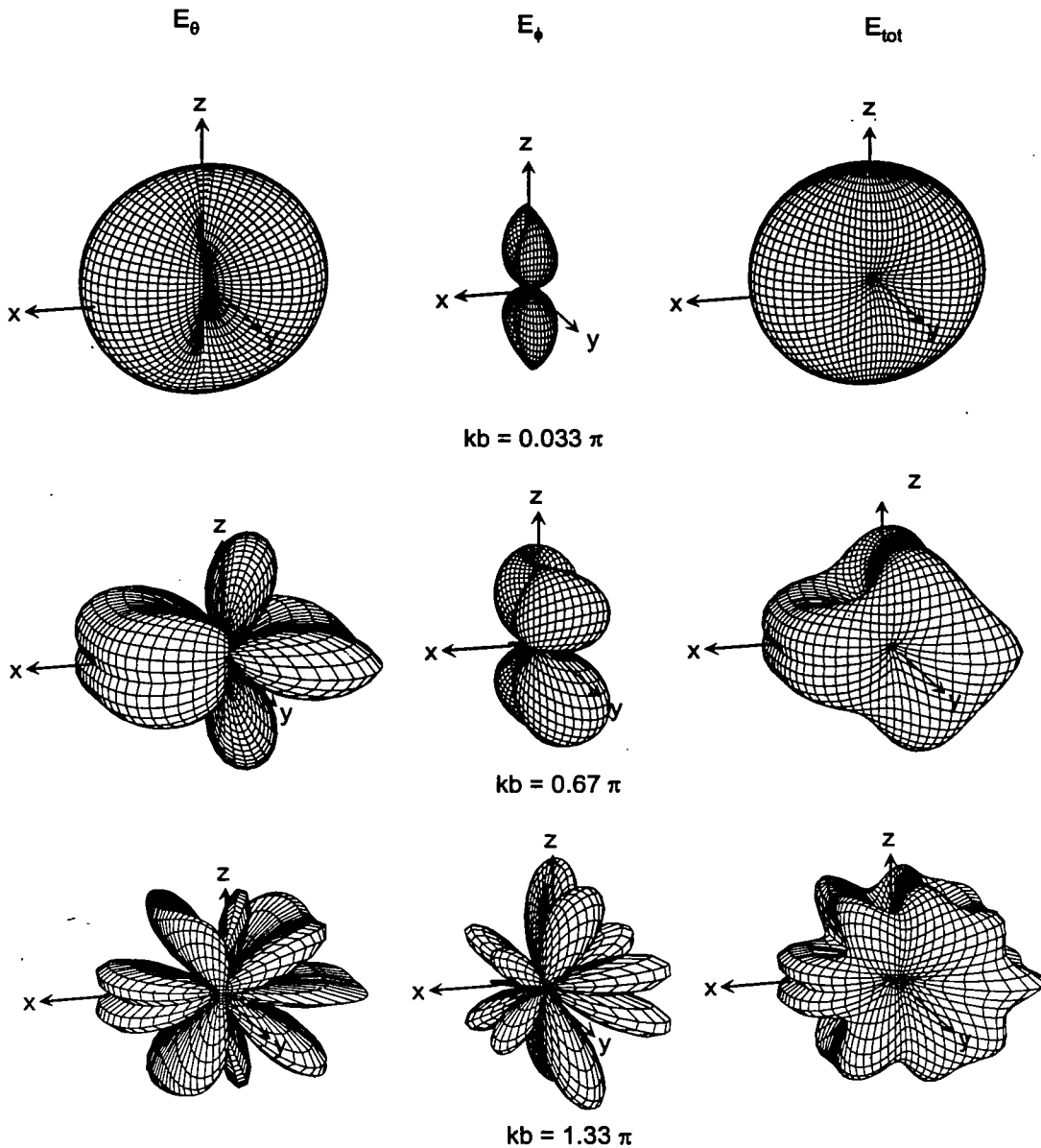


Figure 14. Far field radiation patterns at different normalized frequencies,  $kb$ , for the isolated loop antenna of radius  $b$ .

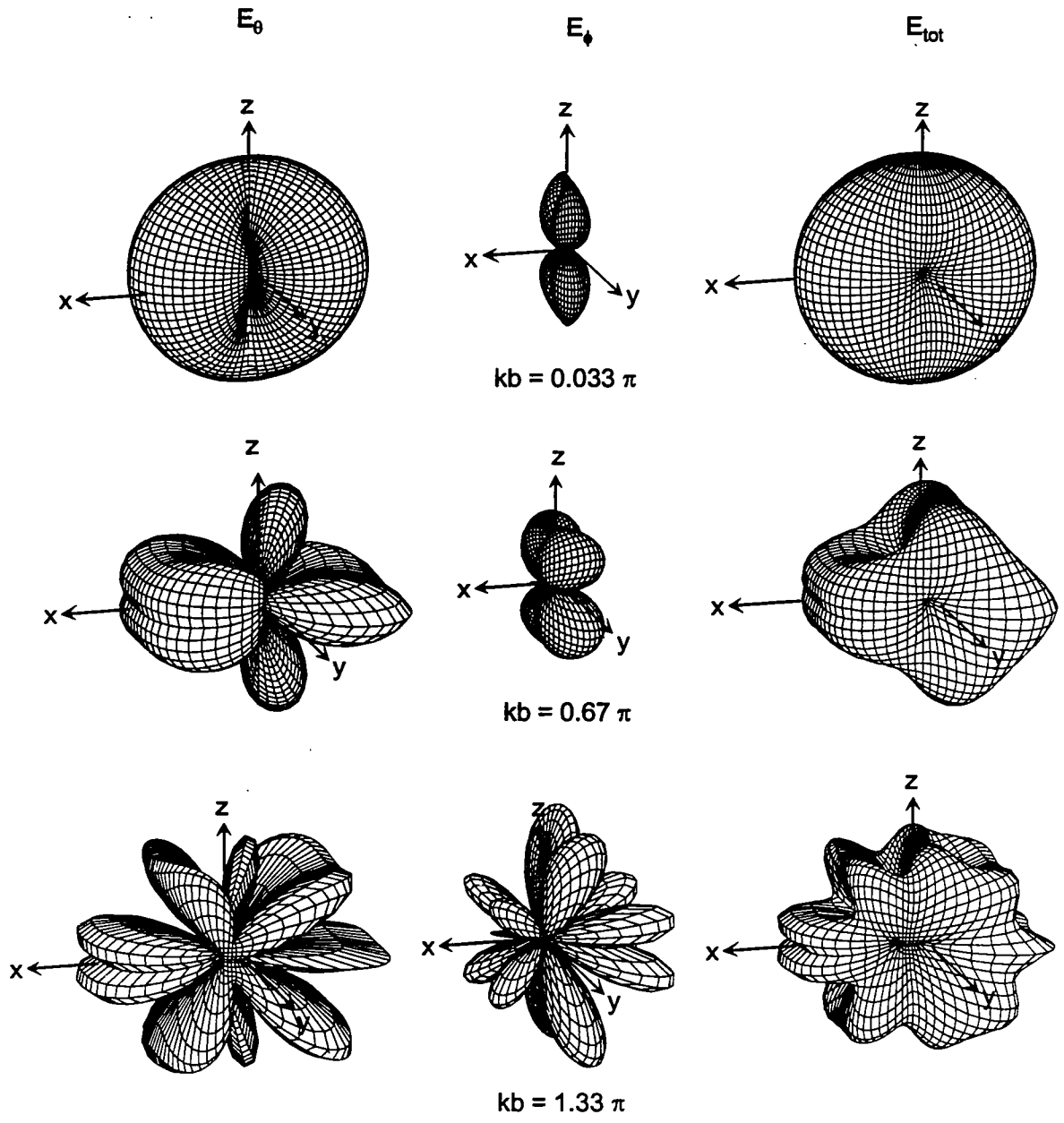


Figure 15. Far field radiation patterns at different normalized frequencies,  $kb$ , for the loop antenna of radius  $b$  with a parasitic wire.

### 3.3 Analysis of the Composite P×M Antenna

For the composite antenna shown in Figure 8, only certain combinations of voltage sources will cause the antenna to radiate as a p×m antenna. Given arbitrary wire and loop excitation voltages,  $V_{Wire}$  and  $V_{Loop}$ , the electric and magnetic dipole moments can be expressed by a linear matrix relationship

$$\begin{bmatrix} p_z \\ m_y \end{bmatrix} = \begin{bmatrix} \kappa_{11} & \kappa_{12} \\ \kappa_{21} & \kappa_{22} \end{bmatrix} \begin{bmatrix} V_{Wire} \\ V_{Loop} \end{bmatrix}, \quad (50)$$

where the four coefficients  $\kappa_{ij}$  are to be evaluated from the integral equation solutions. Considering two cases where  $V_{Wire} = 1$  and  $V_{Loop} = 1$  and  $V_{Wire} = -1$  and  $V_{Loop} = 1$  permits the calculation of two sets of different dipole moments ( $p_z^+$  and  $m_y^+$ ) and ( $p_z^-$  and  $m_y^-$ ) using the NEC code<sup>1</sup>. This process results in 2 equations for the 4 unknowns. The other two equations result from the requirement that  $p_z$  and  $m_y$  are related by Eq.(38):

$$p_z = -\frac{m_y}{c}, \quad (51)$$

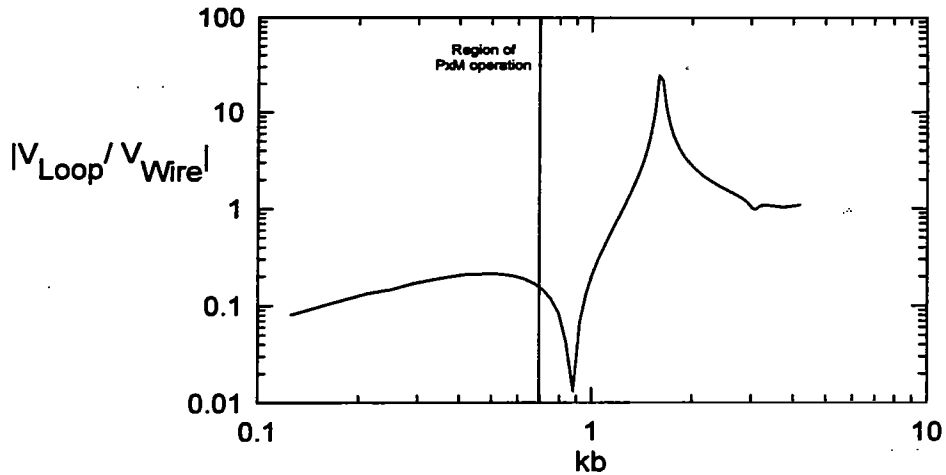
and by a normalizing assumption that

$$V_{Wire} = 1. \quad (52)$$

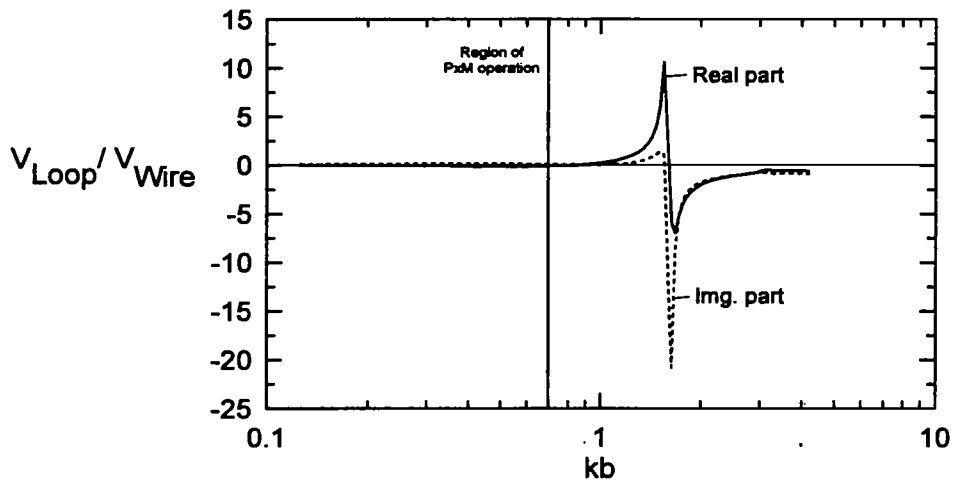
With these 4 equations, the normalized loop voltage  $V_{Loop}/V_{Wire}$  can be evaluated. Note that because the mutual coupling between the wire and loop antennas changes with the frequency, the required normalized loop voltage is frequency dependent. Figure 16 presents a plot of the ratio  $V_{Loop}/V_{Wire}$  for the optimal p×m operation of this antenna as a function of normalized frequency  $kb$ . Notice that the region of operation of the antenna is indicated on the plot, and a clear variation of the loop voltage is indicated. At low frequencies, the required loop voltage approaches zero, because the inductive reactance of the loop becomes small and the current grows without bound. Thus, at low frequencies a very small loop voltage can create a large magnetic dipole moment. For other frequencies, the ratio of  $V_{Loop}/V_{Wire}$  must be continuously adjusted as the frequency changes — a requirement that makes this particular antenna difficult for practical use.

---

<sup>1</sup> The NEC code does not compute dipole moments directly. To do this, the NEC code is first run with the appropriate excitation voltages, and the current and charge distributions on the wires determined. Then, a separate program is used to numerically evaluate Eqs.(3) and (22) for the dipole moments.



(a) Magnitude



(b) Real and imaginary parts

**Figure 16.** Plots of the ratio of the loop to wire voltage source strengths for the optimal  $p \times m$  operation of the antenna, shown as a function of normalized frequency  $kb$ .

An alternative view of the excitation of this  $p \times m$  structure is obtained by considering the loop antenna to be excited by a constant current source,  $I_{Loop}$ , as shown in Figure 17. In this manner, the ratio of the excitation loop current source to the wire voltage source will approach a constant value at low frequencies. This behavior is noted in Figure 20 which plots the normalized ratio of the sources,  $Z_0 I_{Loop}/V_{Wire}$ . Here,  $Z_0$  is the impedance of free space ( $\approx 377 \Omega$ ) which has been used for convenience.

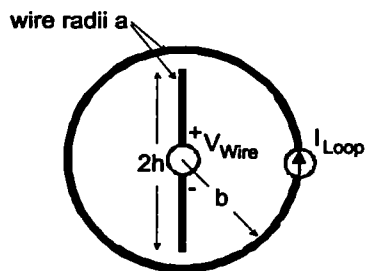
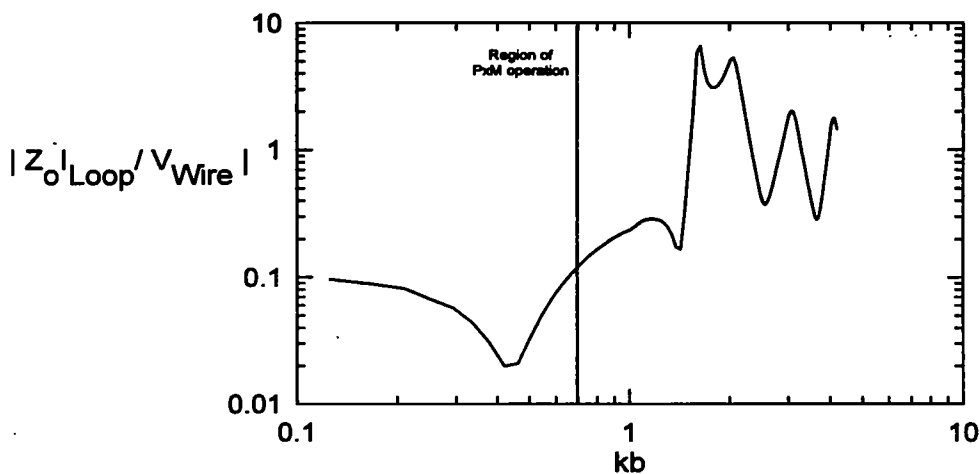
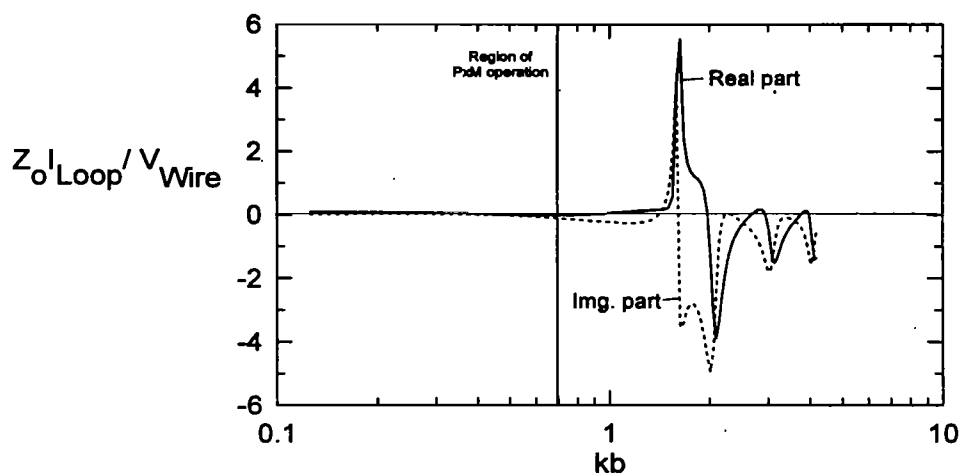


Figure 17. The finite  $p \times m$  antenna with voltage excitation on the linear antenna and current excitation on the loop.



(a) Magnitude



(b) Real and imaginary parts

Figure 18. Plots of the normalized ratio of the loop current source to the wire voltage source for optimal  $p \times m$  operation of the antenna, shown as a function of normalized frequency  $kb$ .

### 3.4 EM Fields Produced by the Wire-Loop Antenna

For the proper  $V_{Loop}/V_{Wire}$  voltage ratios, calculations of the far zone E-fields radiated by the  $p \times m$  antenna have been made, and the results are presented in Figure 19 for normalized frequencies of  $kb = 0.033\pi$ ,  $0.1\pi$ ,  $0.2\pi$ ,  $0.33\pi$ ,  $0.67\pi$  and  $1.33\pi$ . Notice that for low frequencies the field patterns are very similar to the ideal  $p \times m$  dipoles of Figure 4. These plots exhibit a primary  $E_\theta$  field in the  $+x$  direction, with a null in the backward direction. For the secondary  $E_\phi$  component, there is a null in the  $+x$  direction. As the frequency increases, however, the field pattern begins to degenerate into a multiple lobe structure, indicating that higher order multiple moments are present in the current and charge distributions.

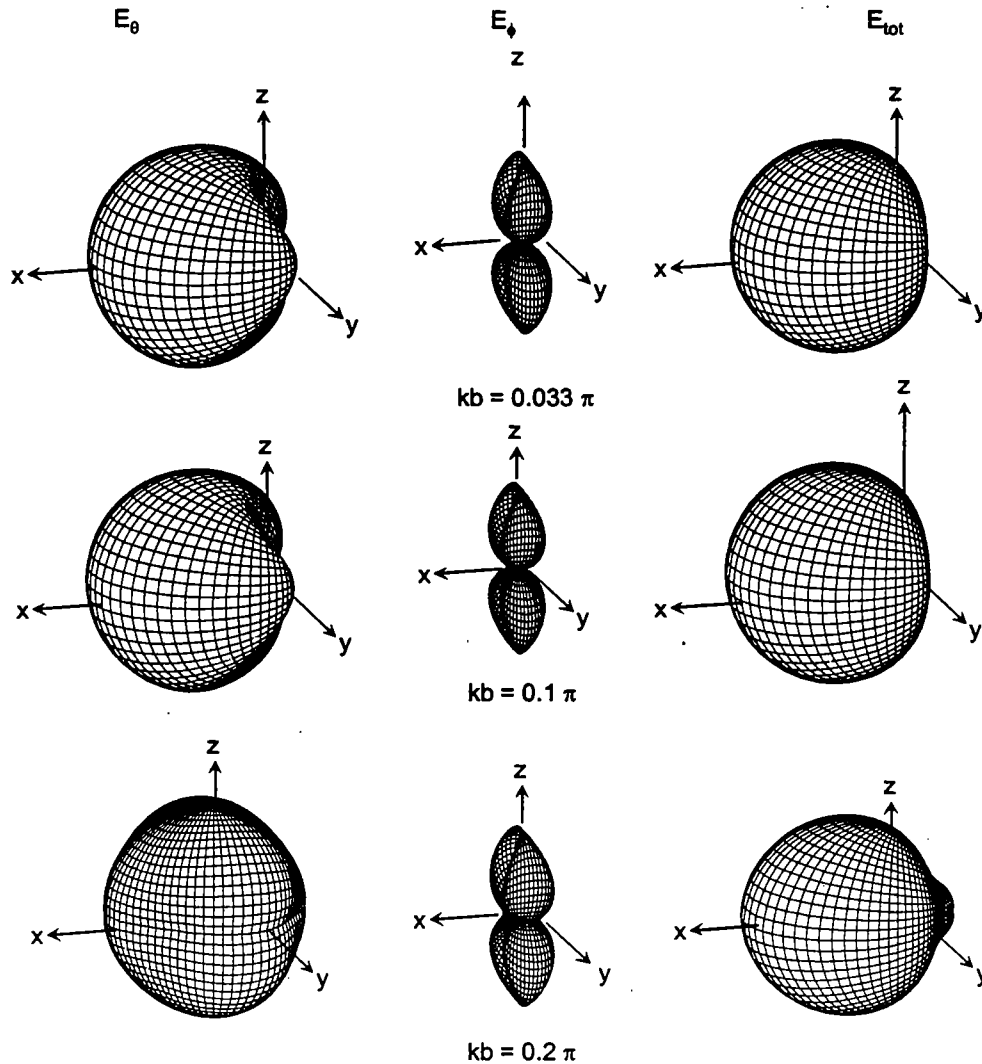
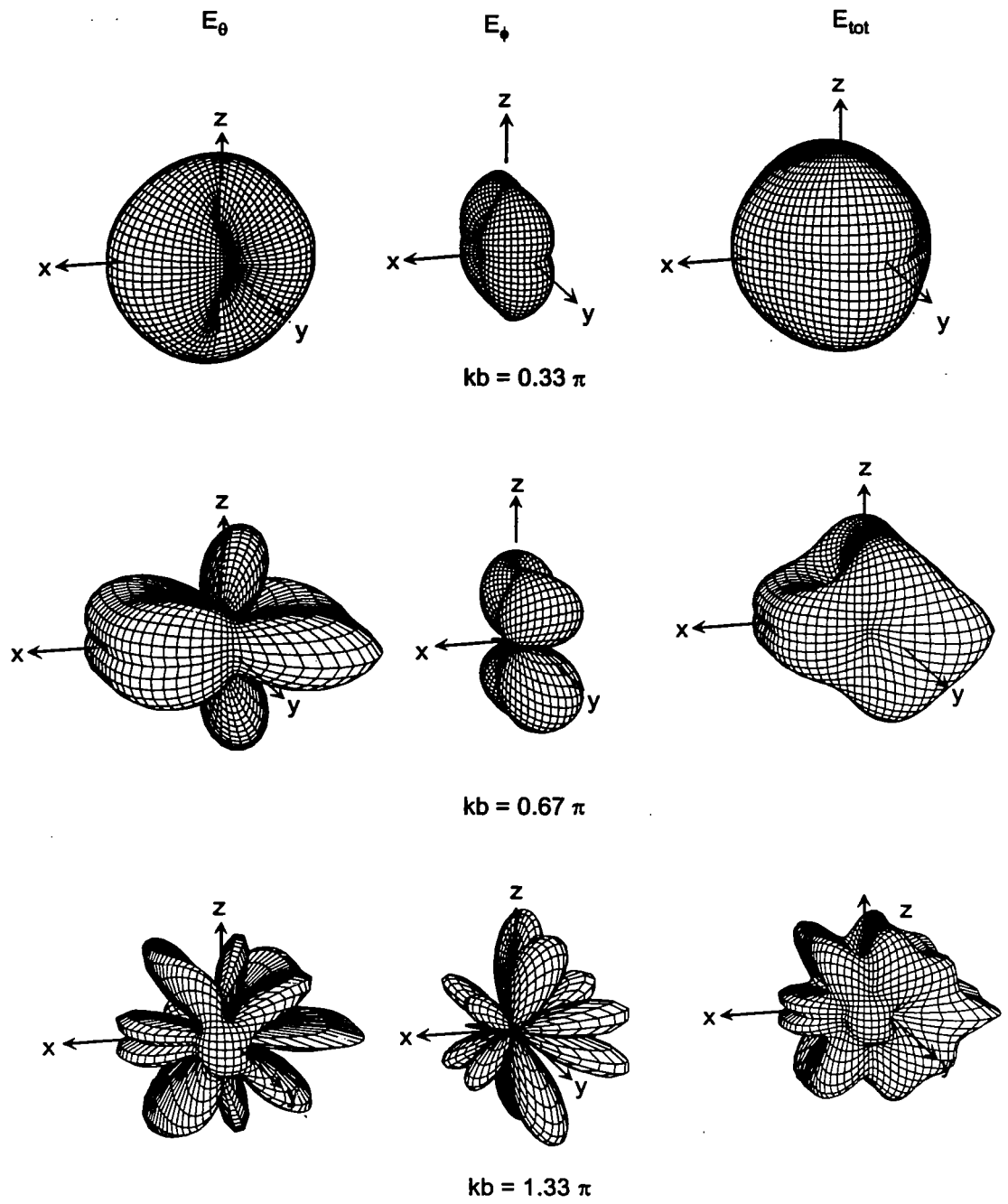


Figure 19. Far zone E-field radiation patterns at different normalized frequencies,  $kb$ , for the wire-loop  $p \times m$  antenna.



**Figure 19. Far zone E-field radiation patterns at different normalized frequencies,  $kb$ , for the wire-loop  $p \times m$  antenna (concluded).**

Of special interest is the operation of this antenna in the low frequency regime where the p×m antenna properties are optimal. Considering a normalized frequency of  $kb = 0.033\pi$  ( $f = 5$  MHz), the ratio of excitation voltages for the p×m operation of the antenna was found to be

$$\frac{V_{Loop}}{V_{Wire}} = -0.01318 + j0.06724.$$

At this frequency, Figure 20 presents the near field  $E_\theta$ ,  $E_\phi$  and  $E_r$  components at various distances from the antenna. Similarly, Figure 21 plots the  $H_\theta$ ,  $H_\phi$  and  $H_r$  near field components. Note the similarity in these plots with those in Figure 4 and Figure 5 for the point p×m antenna. In these plots we note that even at a distance of about 5 times the physical antenna size (i.e., at  $r = 10$  m), the radial component of the field is large. However, along the  $x$ -axis where the principal field components are the largest, both the radial and cross polarized field components are nearly zero, indicating that in this direction the fields appear locally like a plane wave.

One of the main advantages of the p×m antenna is that near the antenna the ratio of E/H remains close to the impedance of free space, implying that the fields appear as local plane waves. This behavior was noted in Figure 6 for the idealized point dipoles. For the extended p×m antenna of Figure 8 a similar calculation has been performed, and the results are reported in Figure 22, where plots of the wave impedance  $Z_w^{(v)}$  for the principal  $E_\theta$  and  $H_\phi$  fields produced by the isolated loop, the single wire and the composite p×m antenna at normalized frequency  $kb = 0.033\pi$ .

Notice that there is a non-ideal behavior of the impedance for the p×m antenna arising from the fact that very close to the antenna, the fields of the extended source cannot be represented by a single point dipole. For this case, a spatial distribution of electric and magnetic dipoles is needed. However, at a distance of several loop radii (about 3 meters), the impedance approaches a stationary value — an indication that the fields are close to a plane wave configuration at this distance.

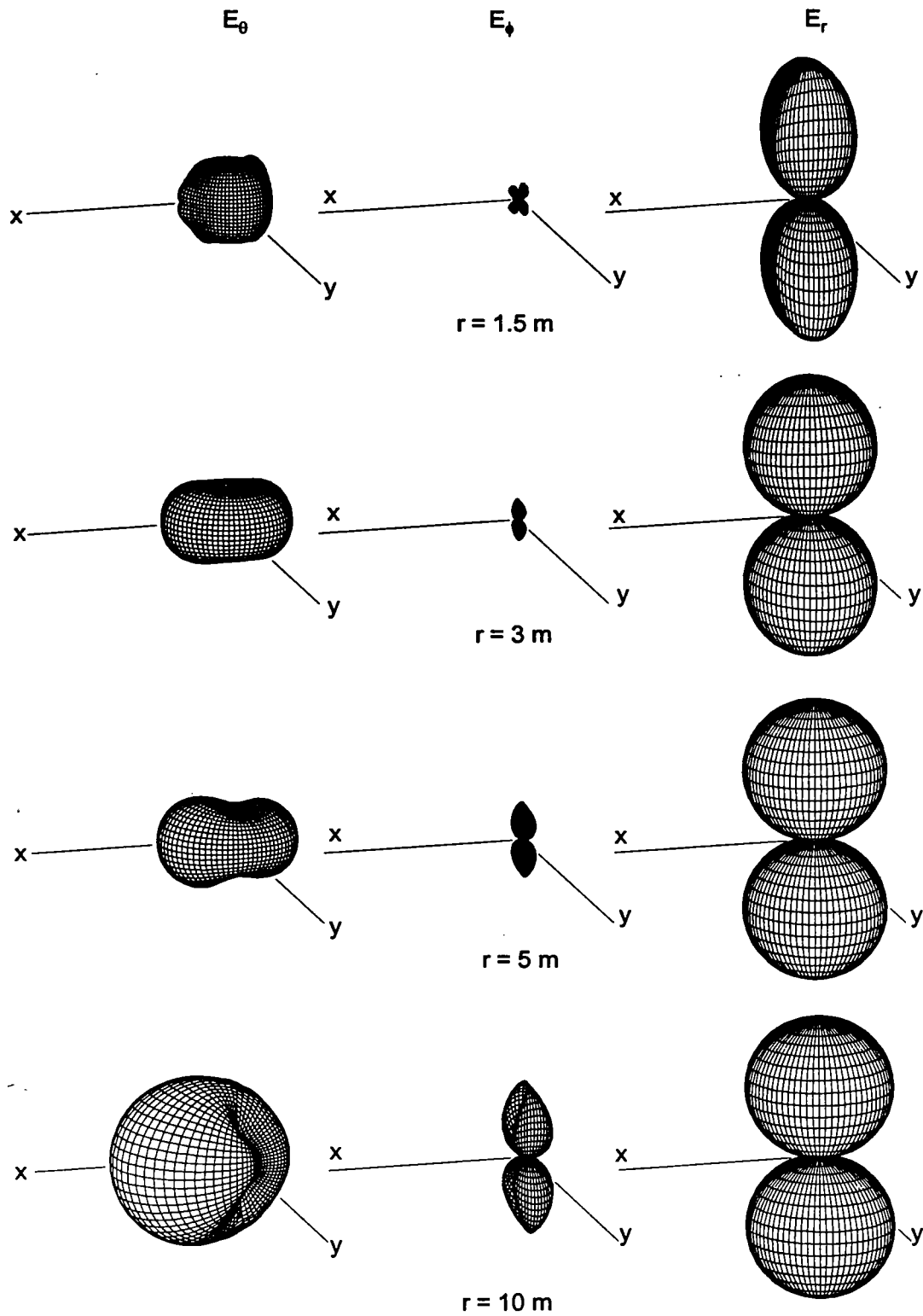
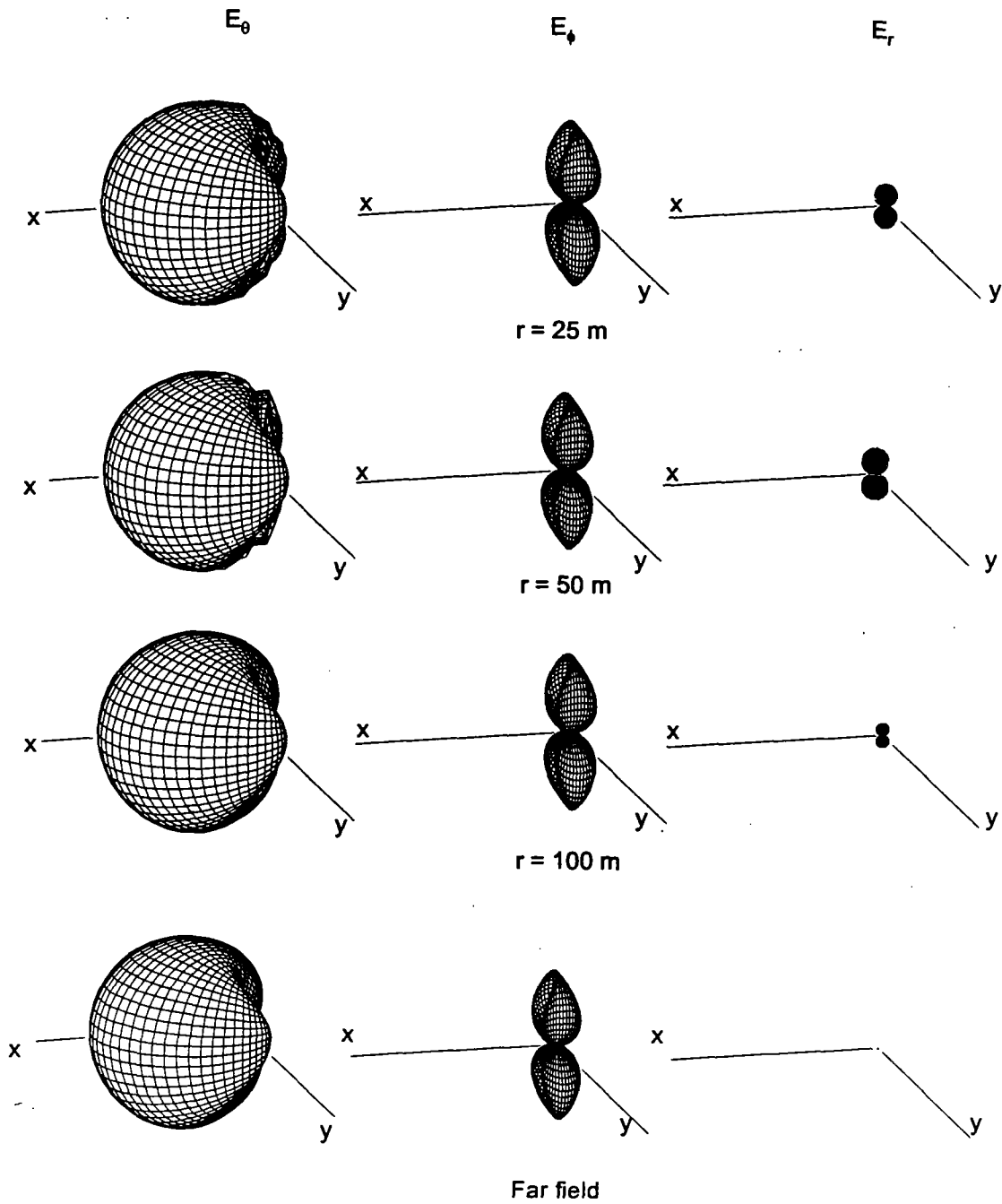
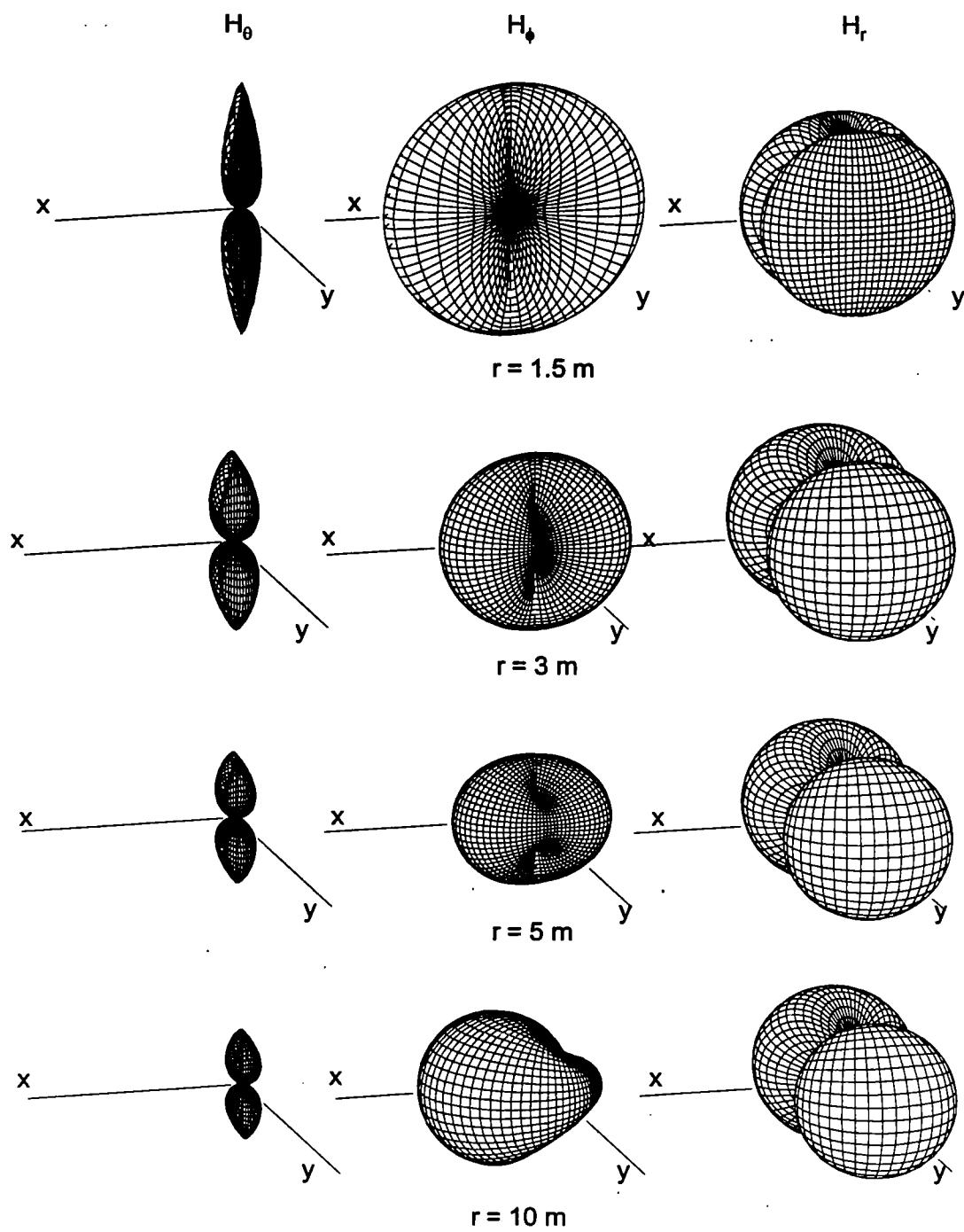


Figure 20. Plots of the  $E_\theta$ ,  $E_\phi$  and  $E_r$  near field components at various distances for a normalized frequency of  $kb = 0.033\pi$ .



**Figure 20. Plots of the  $E_\theta$ ,  $E_\phi$  and  $E_r$  near field components at various distances for a normalized frequency of  $kb = 0.033\pi$ . (concluded).**



**Figure 21.** Plots of the  $H_\theta$ ,  $H_\phi$  and  $H_r$  near field components at various distances for a normalized frequency of  $kb = 0.033\pi$ .

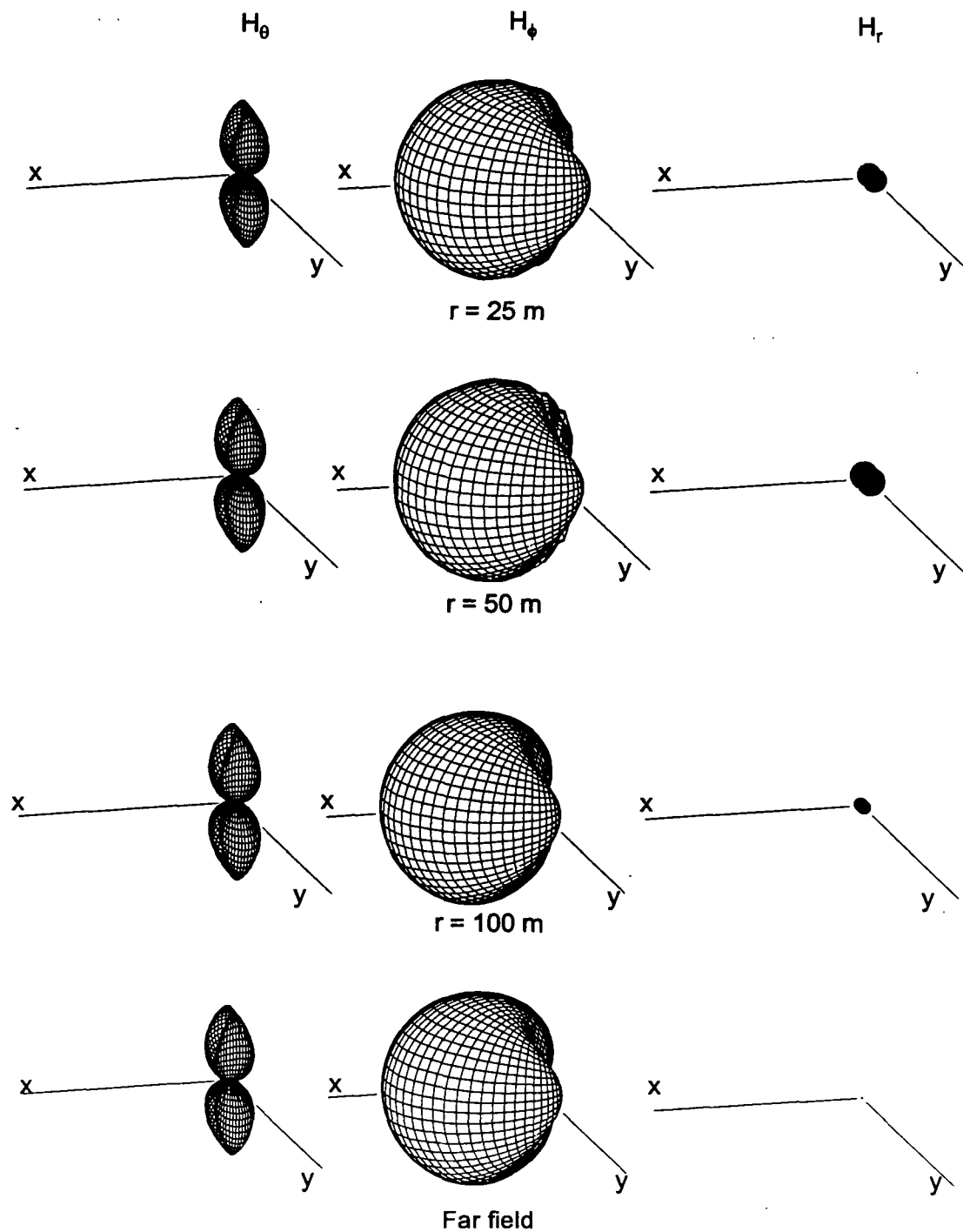
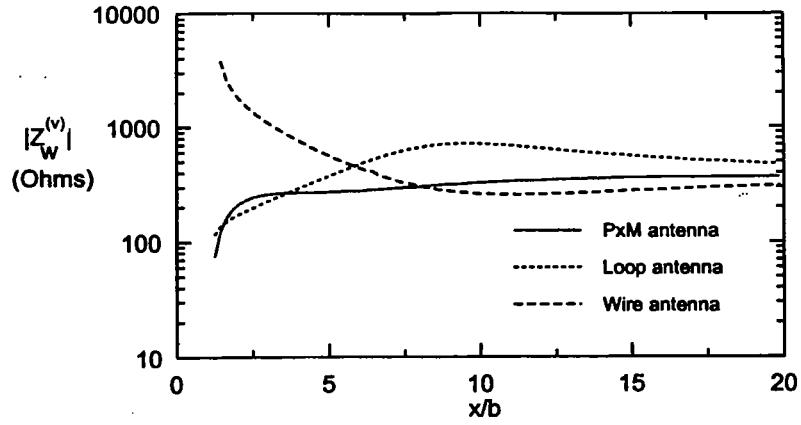
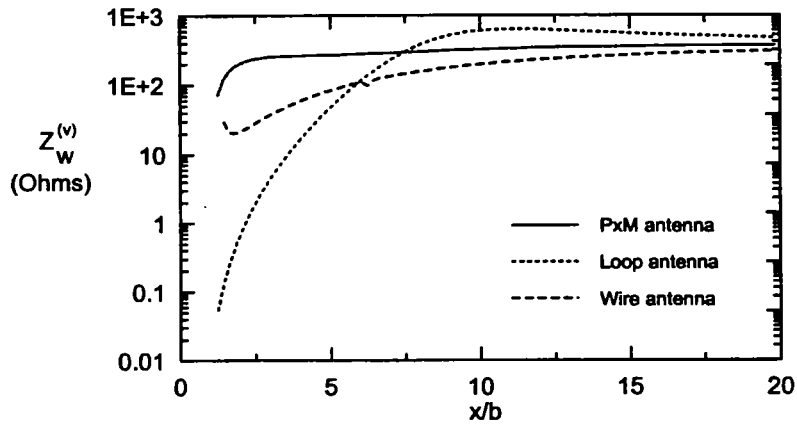


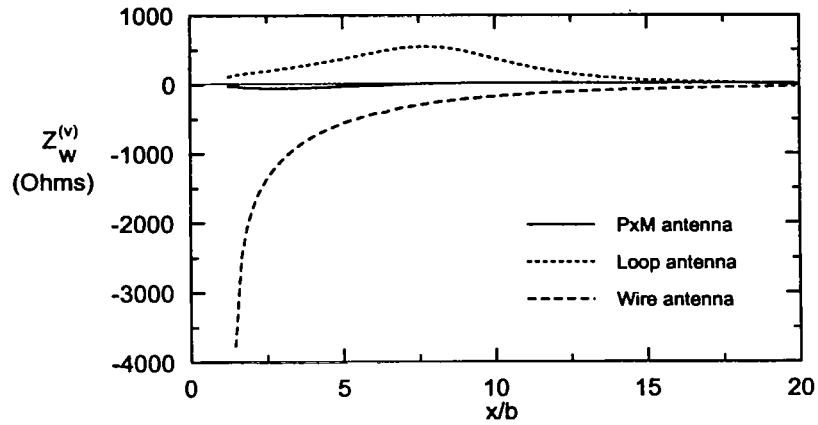
Figure 21. Plots of the  $H_\theta$ ,  $H_\phi$  and  $H_r$  near field components at various distances for a normalized frequency of  $kb = 0.033\pi$  (concluded).



(a) Magnitudes



(b) Real parts



(c) Imaginary parts

Figure 22. Plots of the wave impedance for the principal  $E_\theta$  and  $H_\phi$  fields for the loop, linear element and p×m antenna at normalized frequency  $kb = 0.033\pi$ , as a function of position along the x-axis.

### 3.5 Effects of Impedance Loading

The source excitation models in Figure 8 are unrealistic because most physical sources will have a non-zero internal impedance, with a  $50 \Omega$  impedance being a typical value. To examine this case more carefully, the impedance loaded p×m structure shown in Figure 23 has been considered. The wire antenna source impedance was chosen to be a fixed value of  $Z_{Wire} = 50 \Omega$ , and the impedance of the loop source,  $Z_{Loop}$  was permitted to vary. The resulting loop to wire excitation voltage ratio for this case is illustrated in Figure 24 for  $Z_{Loop} = 0, 50, 450$  and  $1000 \Omega$ . Notice that for the case of  $Z_{Loop} = 450 \Omega$  the voltage ratio fluctuation is small, indicating that this may be a reasonable choice of impedance loading in a practical case. Of course, for a real antenna of this type, more extensive calculations would be warranted for a final design. The small imperfections in the results in the vicinity of  $kb = 0.2$  are artifacts of the calculation, arising from inaccuracies in the NEC solution for loop type antennas.

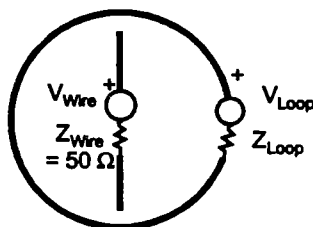


Figure 23. P×M radiating structure with sources with internal impedances  $Z_{Wire}$  and  $Z_{Loop}$ .

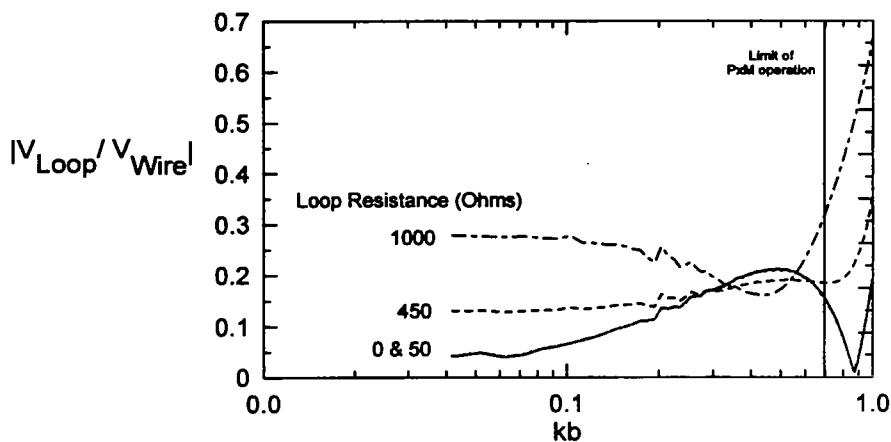


Figure 24. Plot of the ratio of loop to wire voltage for the p×m antenna for various loop source impedances.

It is of interest to examine the frequency domain behavior of the  $E_{\theta}$  field as a function of distance along the  $x$ -axis. Figure 25 shows the normalized E-field magnitude  $|rE_{\theta}/V_{Wire}|$  for the p×m antenna with the loop source impedance  $Z_{Loop} = 450 \Omega$ , the wire source impedance of  $50 \Omega$ , and the loop voltage given by the appropriate data of Figure 24. In this plot, the distance  $r$  is measured along the  $x$ -axis.

Close to the antenna and at low frequencies, the fields approach a constant value which are due to the static fields from the dipoles. Unlike the static fields from a point electric or magnetic dipole, however, the impedance of the fields in this near zone is  $377 \Omega$ . As the frequency increases, the fields approach the far field limit. These result suggests that EM field testing in the near zone can be considered as an alternative to plane wave illumination in the far zone.

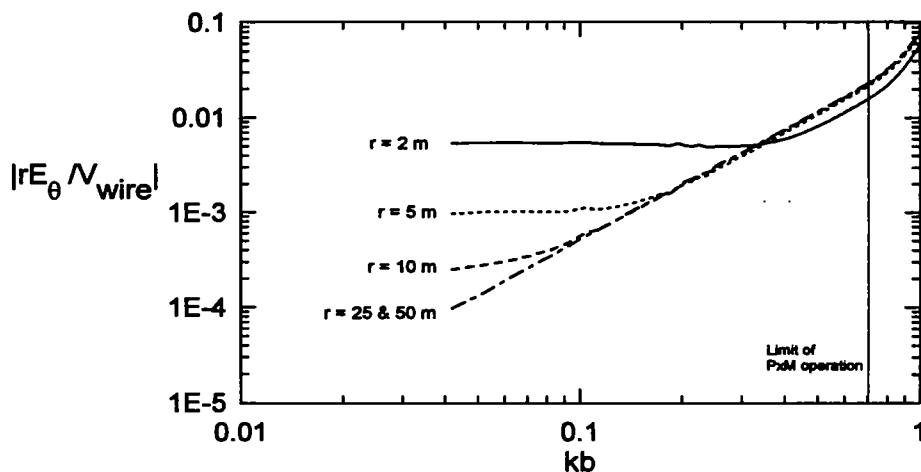


Figure 25. Plot of the normalized frequency dependence of the normalized principal  $E_\theta$  field from the loaded loop-wire  $p \times m$  antenna at various distances along the  $x$ -axis.

### 3.6 Radiation Efficiency

Finally, it is useful to consider the efficiency in the radiation process for the  $p \times m$  antenna. As may be expected, the loading of the antennas by the source impedances will significantly reduce the radiated power, since a large fraction of the available power is absorbed by the impedances. By defining the power delivered by the ideal voltage sources as  $P_{in}$  and the total radiated power from the antenna as  $P_{rad}$ , Figure 26 presents the radiation efficiency defined as

$$Eff = \frac{P_{rad}}{P_{in}} \times 100\%. \quad (53)$$

At low frequencies, this antenna is seen to be very inefficient in its radiation, a price that must be paid to have the desired plane wave characteristics in the near field.

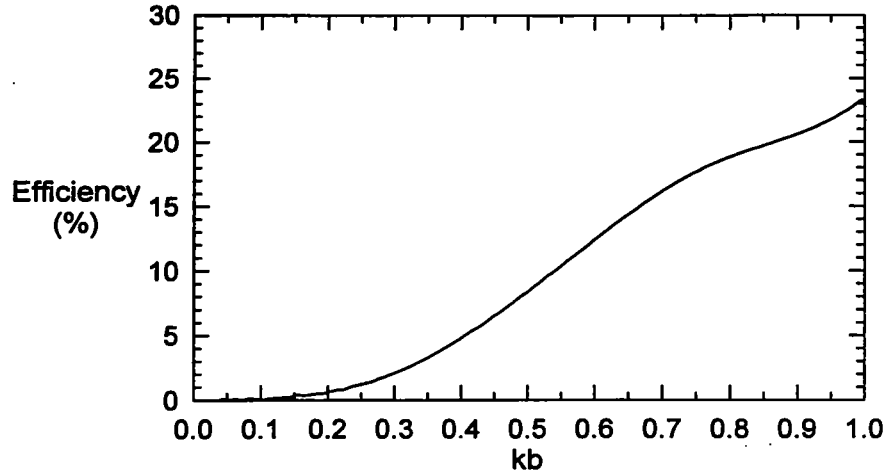


**Figure 26. Radiation efficiency of the loaded  $p \times m$  antenna as a function of normalized frequency  $kb$ .**

#### **4. The Transmission Line $P \times M$ Antenna**

Although the wire-loop combination discussed in the previous section yields the proper field behavior and other radiating characteristics of a  $p \times m$  antenna, there are practical difficulties in its realization:

- The antenna requires two voltage sources, one of which must track the other with a specific complex voltage ratio  $V_{Loop}/V_{wire}$  as the frequency changes.
- The antenna is located in free space and any power cables or feeding conductors from the two sources will couple to the antenna structure and adversely affect the  $p \times m$  antenna radiation.
- The strong mutual coupling between the antenna elements makes it difficult to design other realizations of this type of antenna without the use of extensive numerical calculations.

As a result of these difficulties, it is useful to consider other types of  $p \times m$  antenna structures, one of which is a transmission line antenna. This structure has been discussed in [3], and like the wire-loop structure, under low frequency operation, this antenna can be used to radiate  $p \times m$  fields if certain conditions are met. This antenna will be discussed in the following subsections, with detailed field and impedance plots being developed.

##### **4.1 Antenna Geometry**

The transmission line antenna under discussion here is illustrated in Figure 27. This antenna consists of a conductor of radius  $a$  and length  $L$  over a perfectly conducting

ground plane. It is fed by a voltage source  $V_0$  at the  $x = L$  end of the line, and has a terminating impedance  $Z_L$  at the  $x = 0$  end.

Known as the "Beverage antenna" [22, 23], this is a traveling wave structure and at high frequencies (when  $\lambda < L$ ), it produces an end-fire radiation field in the  $-x$  direction. However, at low frequencies (when  $\lambda > L$ ), the radiation characteristics of this antenna are different, with the main beam of the fields occurring in the  $+x$  direction. If the termination impedance is chosen properly, it has the desired  $p \times m$  radiation characteristics.

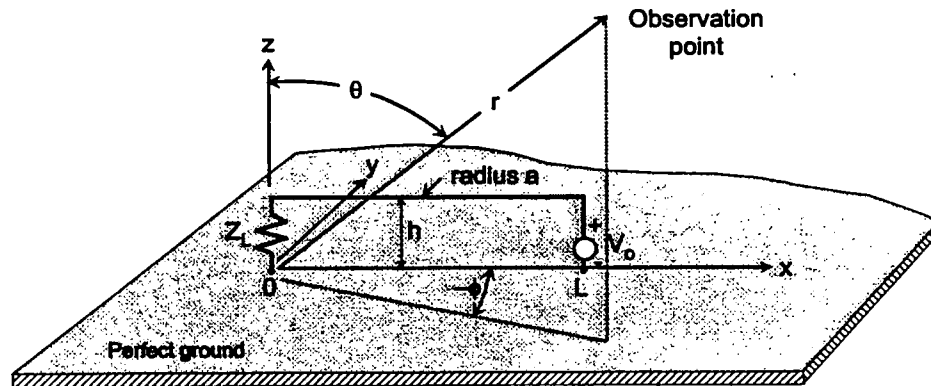
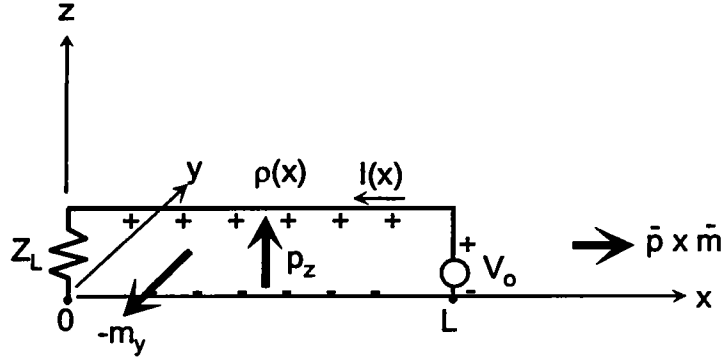


Figure 27. Geometry of the transmission line  $p \times m$  antenna.

## 4.2 Analysis Methods

### 4.2.1 Transmission line model

The low frequency radiating behavior of this antenna can be explained much in the same way as for the wire-loop structure. The voltage source induces a current  $I$  in the conductor with a return through the ground plane connection. This creates a magnetic dipole moment  $-m_y$ , as pictured in Figure 28. In addition, the source induces a positive charge on the top wire and a negative charge on the ground plane (or equivalently, on the image of the wire in the ground), and this creates an electric dipole moment  $p_z$ . The  $p \times m$  combination of these dipole moments is a vector in the  $+x$  direction, indicating that the low frequency radiation from this antenna will be backfire — away from the line at the source end.



**Figure 28. Induced current, charge and dipole moments on the transmission line  $\mathbf{p} \times \mathbf{m}$  antenna.**

While not an exact theory, transmission line modeling of this antenna allows a straightforward understanding of its characteristics [18]. The induced current on the transmission line can be approximated by a forward and backward traveling wave of the form

$$I(x) = a_1 e^{-jkx} + a_2 e^{+jkx} \quad (54)$$

where  $a_1$  and  $a_2$  are unknown constants determined by the excitation and loading conditions on the line, and  $k = 2\pi f/c$ .

The charge on the line is related to the current distribution through the continuity equation

$$-j\omega\rho(\vec{r}) = \nabla \cdot \mathbf{J}(\vec{r}), \quad (55a)$$

which for this 2-dimensional problem becomes

$$-j\omega\rho(x) = \frac{dI(x)}{dx} = -jk[a_1 e^{-jkx} - a_2 e^{+jkx}] \quad (55b)$$

or

$$\rho(x) = \frac{1}{c} [a_1 e^{-jkx} - a_2 e^{+jkx}]. \quad (56)$$

To obtain a  $\mathbf{p} \times \mathbf{m}$  radiating condition, consider matching the line at  $x = 0$  by setting the load impedance to the characteristic impedance of the transmission line:

$$Z_L = Z_c = \sqrt{\frac{L'}{C}} = \frac{Z_0}{2\pi} \ln\left(\frac{2h}{a}\right) \quad (57)$$

where  $L'$  and  $C'$  are the per-unit-length inductance and capacitance of the line and  $Z_o$  is the free space wave impedance introduced earlier. For this matched load there is no reflected wave from the load end of the line. With the voltage excitation at  $x = L$ , both the current and charge are represented by negative traveling waves of the form:

$$I(x) = -\frac{V_o}{Z_L} e^{jk(x-L)} \quad (58a)$$

$$\rho(x) = \frac{1}{c} \frac{V_o}{Z_L} e^{jk(x-L)}. \quad (58b)$$

From these current and charge distributions, the dipole moments of Eqs.(3) and (22) can be evaluated by a direct integration. At frequencies sufficiently low so  $kL \ll 1$ , the exponential terms in Eq.(58) are unity and the dipole moments are given as

$$p_z \approx \int_0^L \rho(x) 2h dx = \frac{1}{c} \frac{V_o}{Z_L} 2A_{Loop} \quad (59)$$

$$m_y \approx -\int_0^L I(x) 2h dx = -\frac{V_o}{Z_L} 2A_{Loop}, \quad (60)$$

where  $A_{Loop} = hL$  is the area of the loop formed by the transmission line conductor and the ground surface.

Note that in this case, the relationship between  $p_z$  and  $m_y$  is identical to the  $p \times m$  condition of Eq.(38), and we expect that at low frequencies and for distances far from this antenna, the fields will be like those from the ideal point  $p \times m$  source. However, near the antenna or at higher frequencies, we will expect deviations from this ideal source behavior, much as encountered for the wire-loop radiator.

Note that the simple transmission line analysis neglects the contributions to the dipole moments from the currents and charges flowing in the vertical ends of the line. As discussed in [3], however, such contributions are not very important (see Figure 4 on page 31) and do not add to the basic understanding of this antenna operation. While transmission line modeling techniques could be applied to include these effects [24], this has not done here.

#### 4.2.2 Integral equation model

Aside from the errors in the transmission line model discussed in the previous section in not accounting for the effects of the vertical ends of the line, there is another fundamental error in such a model: it does not properly account for radiation losses. As a result, the current and charge distributions on the line as computed from the transmission line model are not correct. However, as mentioned in [18], the errors in these

distributions for a line over a perfect ground plane as in Figure 27 are not too large, and the resulting solutions are usually acceptable.

For a more accurate solution for this antenna, an integral equation solution is possible. Once again the NEC code may be used to evaluate the current and charge distributions, along with the radiation and near zone fields. As in the previous case of the wire-loop structure, care must be used in running this code — especially if the structure being modeled contains loops as they can cause spurious “noise” in the solution at low frequencies.

As a check of the validity of the analysis and stability of the solution, the input admittance (or impedance) of the antenna is a good quantity to calculate and plot. Consider the case of a transmission line antenna having the following dimensions:

Wire length  $L = 30$  m  
 Height over ground  $h = 3$  m  
 Conductor radius  $a = 0.1$  cm

For this structure, Figure 29 presents the magnitude of the input admittance as a function of normalized frequency  $kL$  and for different values of the termination impedance  $Z_L$ . For either the nearly open circuited or short circuited cases, there are high resonance peaks and antiresonance nulls, arising from reflections of the traveling waves on the line. The electrically matched case, for which  $Z_L \approx 522 \Omega$ , is seen to provide a very smooth admittance function through the first few resonances, but at the higher frequencies, small variations of the admittance are present. These are due to the effects of the vertical risers in the solution and to the radiation effects becoming important in the solution.

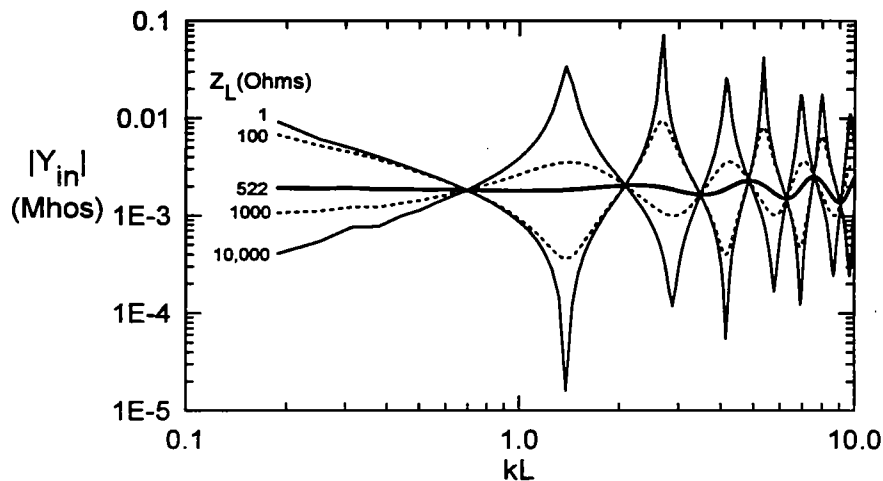


Figure 29. Computed input admittance magnitude of the transmission line  $p \times m$  antenna using an integral equation analysis.

### 4.3 EM Fields from the Transmission Line Antenna

Selecting the load impedance  $Z_L = 522 \Omega$ , a series of calculations were performed to illustrate the E and H fields under different conditions. Figure 30 presents the far zone E-field radiation patterns for this antenna for different values of the normalized frequency,  $kL$ . In these plots, the bottom half of the patterns shown in the plots for the wire-loop antenna of the previous section are not present because of the fields within the perfect ground plane are zero.

The EM fields produced by this antenna are very similar to those of the ideal point  $p \times m$  source and the wire-loop antenna. At low frequencies, the now familiar  $p \times m$  pattern of the principal  $E_\theta$  field component is evident, with a small cross polarized  $E_\phi$  field that vanishes along the  $+x$  axis. The pattern degenerates into higher order multipole lobes as the frequency increases and the line length becomes comparable to a wavelength. For electrically long lines, the Beverage radiation pattern results.

The development of the near fields into the far zone pattern is illustrated in Figure 31 and Figure 32 for the E-fields and H-fields, respectively, for a frequency of  $f = 1$  MHz, corresponding to  $kL = 0.2\pi$ . Note that the distance  $r$  in the figures is measured from the coordinate system center. Thus, a value of  $r = 30$  m will pass through the voltage source at the end of the line. The closest distance to the antenna that has been examined for these calculations is for  $r = 35$  m — corresponding to a distance of 5 m from the  $x = L$  end of the line.

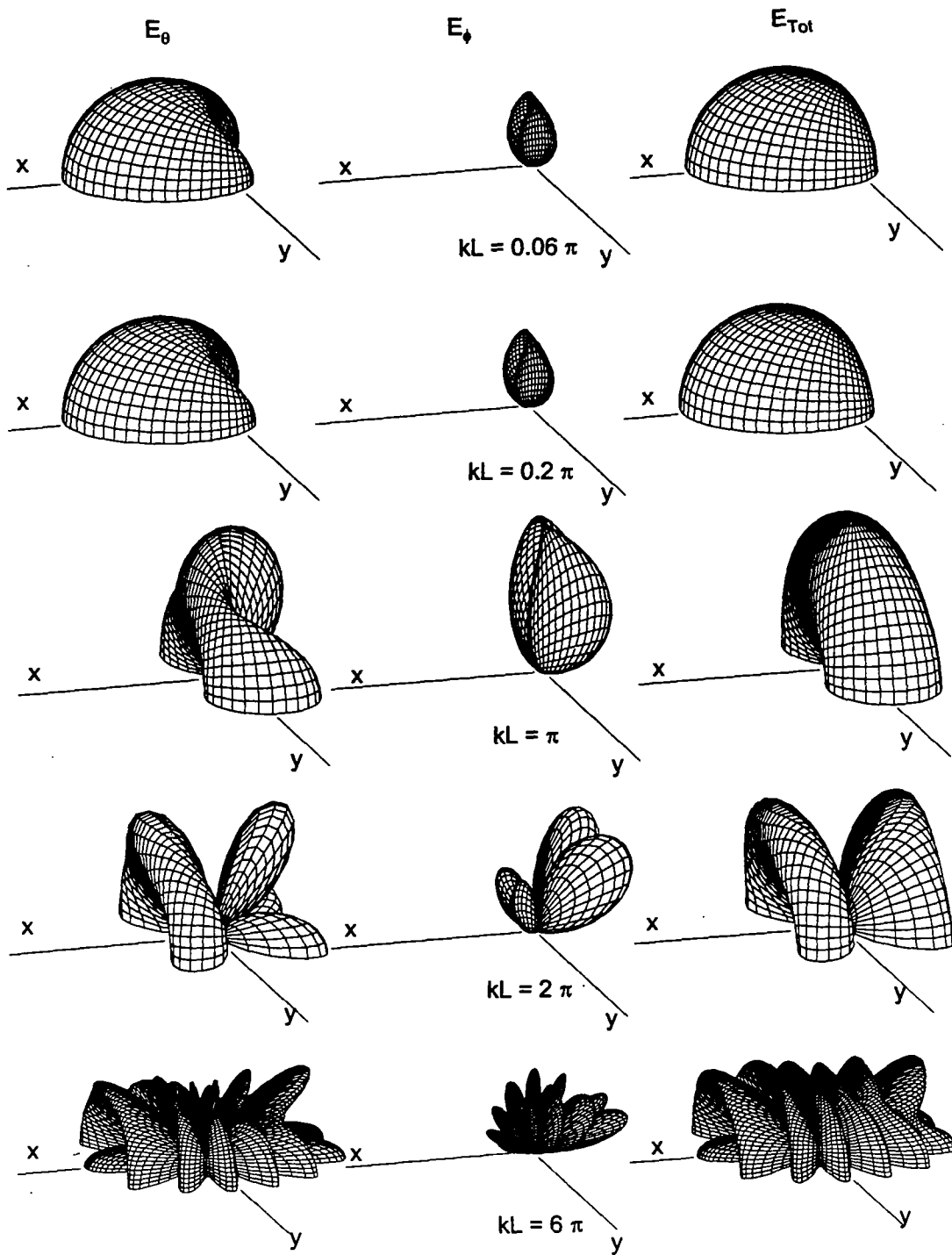


**Figure 30. Far field radiation patterns for the transmission line  $p \times m$  antenna as a function of normalized frequency,  $kL$ .**

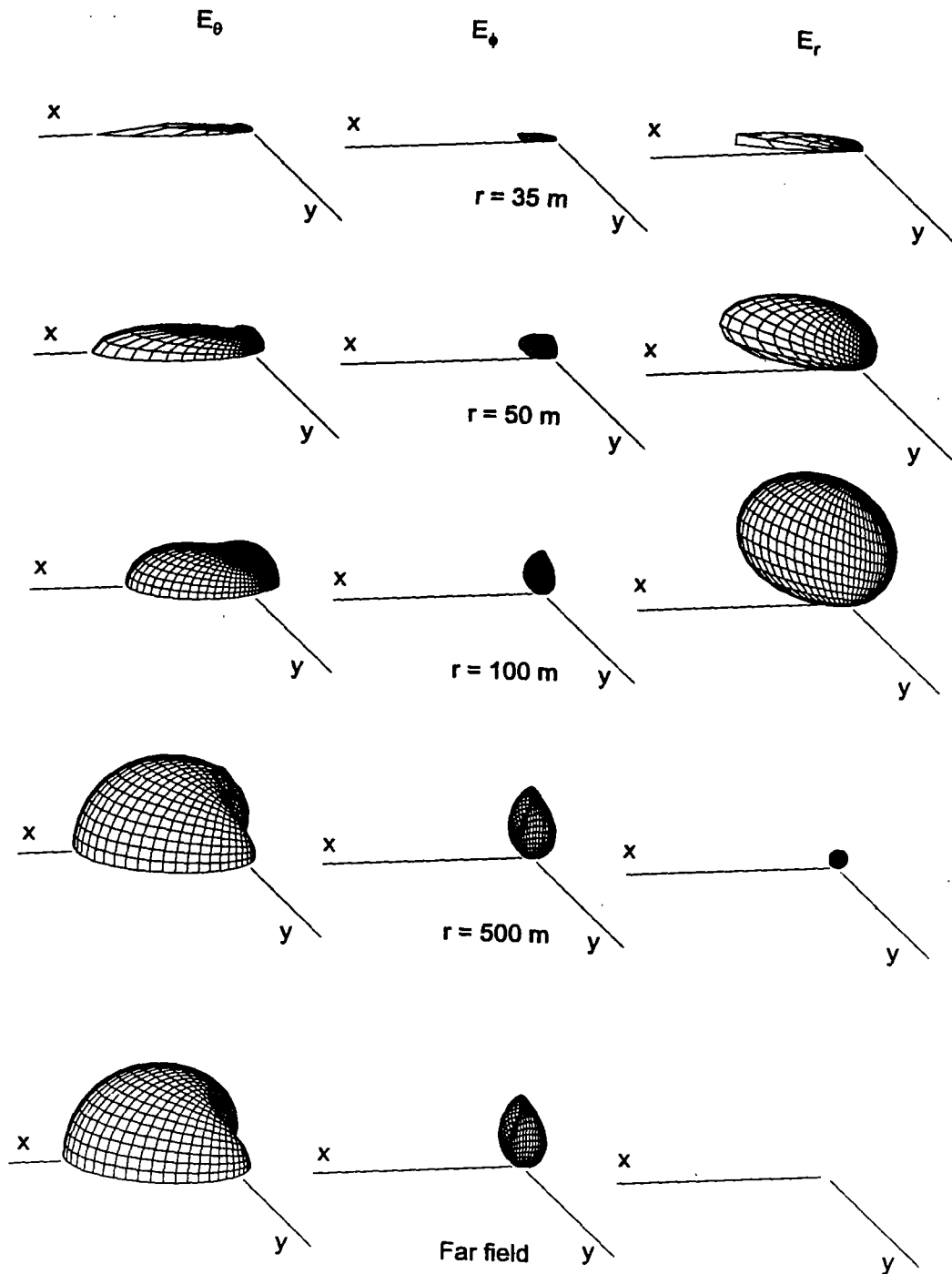


Figure 31. Plots of the  $E_\theta$ ,  $E_\phi$  and  $E_r$  near field components at various distances  $r$  for a normalized frequency  $kL = 0.2\pi$  ( $f = 1\text{ MHz}$ ).

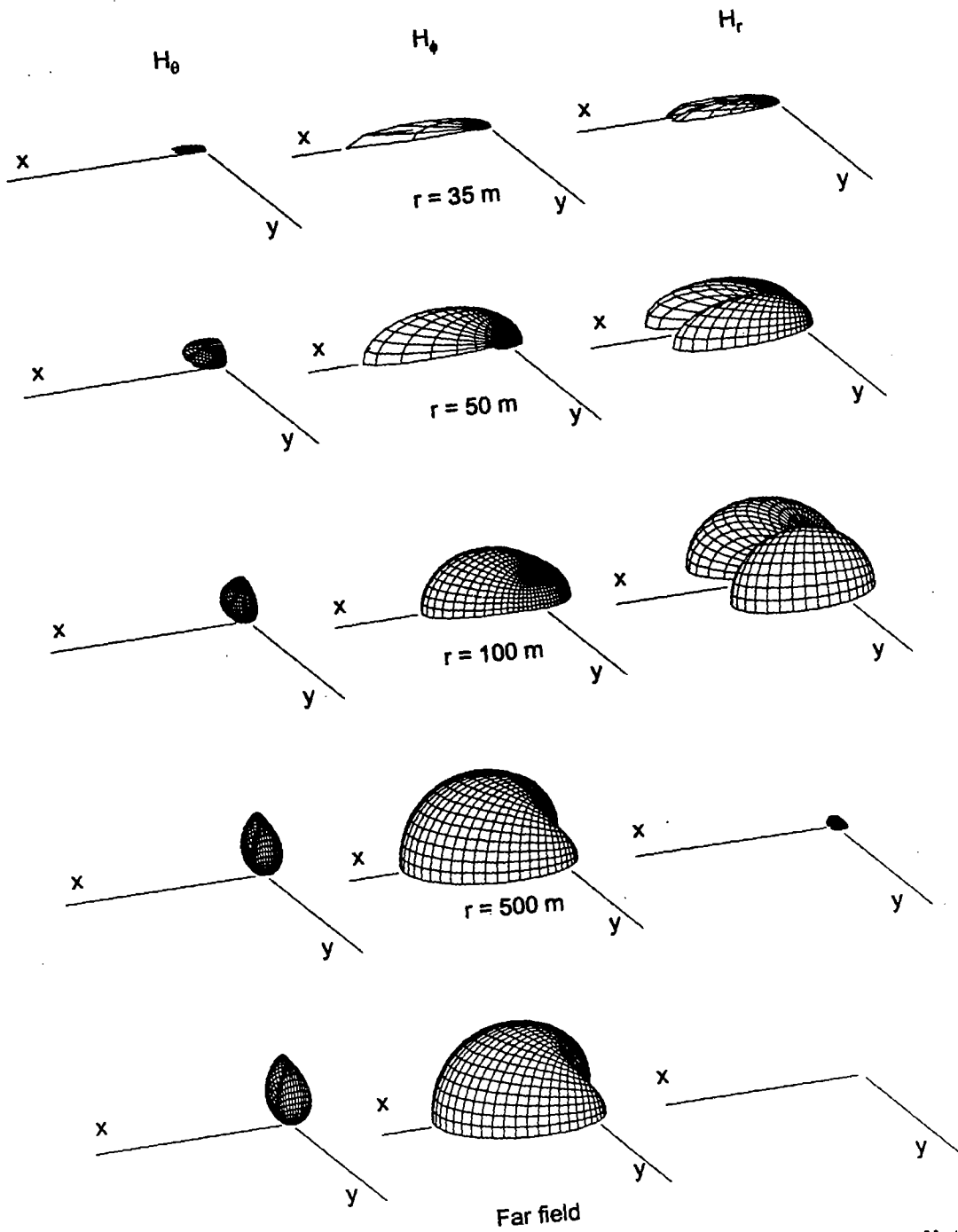


Figure 32. Plots of the  $H_\theta$ ,  $H_\phi$  and  $H_r$  near field components at various distances  $r$  for a normalized frequency  $kL = 0.2\pi$  ( $f = 1$  MHz).

For observation locations closer than about 300 to 500 m (i.e., a distance of about  $10L$ ) the radial field components still have appreciable values. However, along the  $+x$  axis, the ratio of the primary fields  $E_\theta/H_\phi$  is expected to be close to the value of  $Z_o \approx 377\Omega$ . Figure 33 illustrates the wave impedance magnitude  $|Z_w^{(v)}|$  for these components as a function of the position  $x/L$  along the  $+x$  axis, for three different values of normalized frequency  $kL$ . Observe that for low frequencies, a distance of 3 to 4 times the length of the transmission line should be maintained from the voltage source.

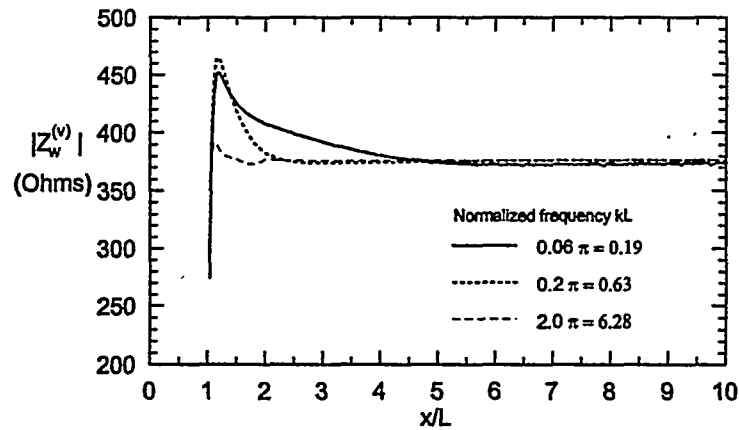


Figure 33. Plot of the wave impedance magnitude for the principal  $E_\theta$  and  $H_\phi$  components produced by the transmission line  $p \times m$  antenna along the  $x$ -axis, for different normalized frequencies  $kL$ .

Finally, the frequency dependence of the principal  $E_\theta$  field at different location along the  $+x$  axis is of interest. Figure 34 presents the normalized E-field magnitude  $|rE_\theta/V_o|$  as a function of normalized frequency  $kL$ . Unlike the point dipole sources, the spectrum of this radiated field is a constant over the range of low frequencies for which the  $p \times m$  radiation occurs.

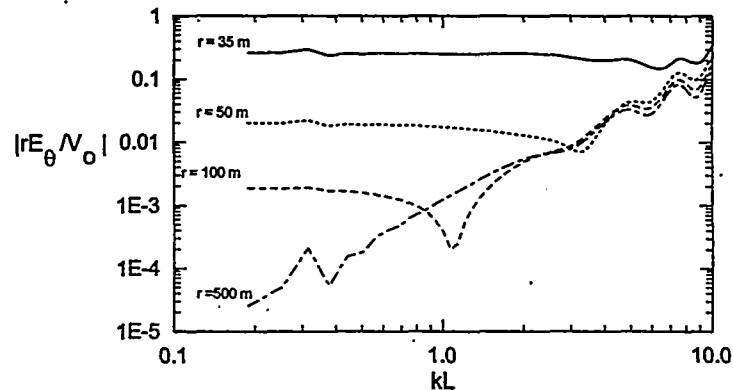


Figure 34. Plot of the normalized  $E_\theta$  field produced by the transmission line  $p \times m$  antenna at various radial distances along the  $x$ -axis, as a function of normalized frequency  $kL$ .

#### 4.4 Radiation Efficiency

As might be expected, the radiation from this antenna is very inefficient. In fact, it is even less efficient than the wire-loop structure because the transmission line structure does not radiate well, even under unloaded conditions. This fact, combined with the added loss in the load impedance at the end of the line, gives rise to a radiation efficiency significantly less than that for the wire-loop. Figure 35 illustrates the computed radiation efficiency for the transmission line antenna, and we note that at a frequency of  $kL = 1$  (about the limit for the  $p \times m$  operation), this antenna has an efficiency of only about 0.15%, while that of the wire-loop structure is about 23%.

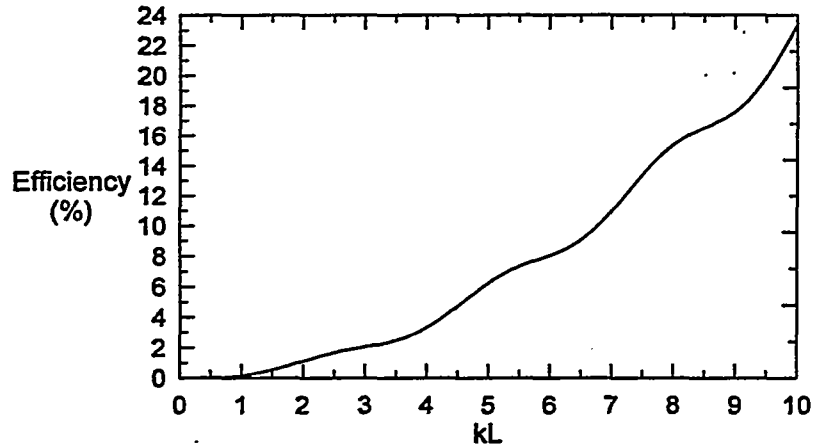


Figure 35. Radiation efficiency of the transmission line  $p \times m$  antenna as a function of normalized frequency  $kL$ .

#### 5. Conclusions

This report has provided a brief overview of the radiation properties of elementary electric and magnetic dipoles. At low frequencies, these sources can be used to approximate the radiation from many different types of antennas.

One particularly useful type of antenna is the  $p \times m$  antenna which contains orthogonal electric and magnetic dipoles having the special relationship  $m_y / c = -p_z$ . In this case, we have noted that the radiation appears to propagate mainly in the  $+x$  direction, with a null in the field in the  $-x$  direction. Moreover, the wave impedance in the forward direction is equal to the impedance of free space ( $377 \Omega$ ) and the power contained in the EM field is entirely real. Away from the  $x$ -direction, this "ideal" behavior of the fields changes and there are variations of the impedance levels as a function of distance from the source and the observation angles. Moreover, the power in the field contains reactive components in other directions.

A disadvantage of this type of antenna, however, is the very low radiating efficiency. A significant amount of energy is lost in the impedance loading placed on the structure to maintain proper  $p \times m$  relationships. Furthermore, parallel conductor

transmission line structures do not radiate well. This implies that a practical design of these antennas must carefully consider the power handling capabilities of the antenna wires, loads and sources. Notwithstanding this difficulty, however, this type of radiating antenna provides a possibility for conducting field illumination tests at low frequencies, primarily due to the ideal behavior of the fields in the  $x$ -direction.

Future work in this area must include the design of a practical  $p \times m$  antennas for use in the field and optimization of the power radiated. Practical details about how the antennas should be constructed and deployed over a lossy earth also need to be addressed. Some of these issues are discussed in a companion SSN note, entitled *The Pxm Antenna and Applications to Radiated Field Testing of Electrical Systems, Part-2 Experimental Considerations*.

## 6. References

1. Tesche, F. M., CW Test Manual, Report written for the NEMP Laboratory, Spiez, Switzerland, December 7, 1994.
2. Baum, C. E., "Some Characteristics of Electric and Magnetic Dipole Antennas for Radiating Transient Pulses, *AFWL Sensor and Simulation Notes*, Note 125, January 1971.
3. Yu, J. S., C-L James Chen and C. E. Baum, "Multipole Radiations: Formulation and Evaluation for Small EMP Simulators", *AFWL Sensor and Simulation Notes*, Note 243, July 19, 1978.
4. Baum, C. E., "Radiation of Impulse-Like Transient Fields", *AFWL Sensor and Simulation Notes*, Note 321, November 25, 1989.
5. Farr, E. G. "Analysis of the Impulse Radiating Antenna, *AFWL Sensor and Simulation Notes*, Note 329, July 24, 1991.
6. Baum, C. E., "General Properties of Antennas", *AFWL Sensor and Simulation Notes*, Note 330, July 23, 1991.
7. Farr, E. G., "Extrapolation of Ground-Alert Mode Data at Hybrid EMP Simulators", *AFWL Sensor and Simulation Notes*, Note 311, July 1988.
8. Farr, E. G., and J. S. Hofstra, "An Incident Field Sensor for EMP Measurements", *AFWL Sensor and Simulation Notes*, Note 319, November 6, 1989.
9. Balanis, C., **Advanced Engineering Electromagnetics**, John Wiley and Sons, New York, 1989.
10. Harrington, R. F., **Time Harmonic Electromagnetic Fields**, McGraw Hill, New York, 1961.
11. Jones, D. S., **The Theory of Electromagnetism**, Pergamon Press, London, 1964.
12. Jordan, E. C., and K. G. Balmain, **Electromagnetic Waves And Radiating System**", Prentice-Hall, Inc., 1968.
13. Plonsey, R. And R. E. Collin, **Principles and Applications of Electromagnetic Fields**, McGraw-Hill Book Co., New York, 1961.
14. Ramo, S., J. R. Whinnery, & T. Van Duser, **Fields and Waves in Communication Electronics**, Second Edition. John Wiley and Sons, 1989.

15. Stratton, J. A., **Electromagnetic Theory**, McGraw-Hill Book Co., New York, 1941.
16. Van Bladel, J., **Electromagnetic Fields**, McGraw Hill, New York, 1964.
17. Jackson, J. D., **Classical Electrodynamics**, Second Ed., John Wiley & Sons, New York, 1975.
18. Tesche, F. M., M. V. Ianoz and T. Karlsson, **EMC Analysis Methods and Computational Models**, John Wiley & Sons, New York, 1996.
19. Johnk, C. T. A., **Engineering Electromagnetic Fields and Waves**, John Wiley & Sons, New York, 1988.
20. Harrington, R. F., **Field Computation by Moment Methods**, reprinted by the author, 1968.
21. Burke, G.J., and A.J. Poggio, "Numerical Electromagnetics Code (NEC) - Method of Moments", NOSC TD 116, January 1981.
22. Johnson, R. C., and H. Jasik, **Antenna Engineering Handbook**, McGraw-Hill, New York, 1961.
23. Stutzman, W. L., and G. A. Thiele, **Antenna Theory and Design**, John Wiley & Sons, New York, 1981.
24. Tesche, F.M. and B. R. Brändli, "Observations on the Adequacy of Transmission Line Coupling Models for Long Overhead Cables", *Proceedings of the International Symposium on EMC, EMC'94 ROMA*, Sept. 13-16, 1994